ADVANCING EARTH AND SPACE SCIENCE

Water Resources Research

RESEARCH ARTICLE
10.1029/2020WR029494

Key Points:

- Multi-dimensional coherent vortices in a partially obstructed channel with a submerged canopy were visualized and analyzed
- Scalings of velocity and Reynolds stress in multi-dimensions based on experimental data were conducted and discussed
- Momentum exchange governed by secondary flows and vortices was investigated to understand hydrodynamics in a partially obstructed channel

Supporting Information:

Supporting Information may be found in the online version of this article.

Correspondence to:

X.-K. Wang,
wangxiekang@scu.edu.cn

Citation:

Yan, X.-F., Duan, H.-F., Wai, W.-H. O., Li, C.-W., & Wang, X.-K. (2022). Spatial flow pattern, multidimensional vortices, and junction momentum exchange in a partially covered submerged canopy flume. *Water Resources Research*, *58*, e2020WR029494. https://doi.org/10.1029/2020WR029494

Received 20 DEC 2020
Accepted 21 FEB 2022

Author Contributions:

Conceptualization: Xu-Feng Yan, Huan-Feng Duan, Wing-Hong Onyx Wai, Chi-Wai Li, Xie-Kang Wang
Data curation: Xu-Feng Yan
Funding acquisition: Xu-Feng Yan, Huan-Feng Duan, Xie-Kang Wang
Investigation: Xu-Feng Yan
Methodology: Xu-Feng Yan, Huan-Feng Duan, Wing-Hong Onyx Wai
Resources: Xie-Kang Wang
Software: Xu-Feng Yan
Supervision: Huan-Feng Duan, Wing-Hong Onyx Wai, Xie-Kang Wang
Validation: Xu-Feng Yan
Visualization: Xu-Feng Yan
Writing – original draft: Xu-Feng Yan

Spatial Flow Pattern, Multi-Dimensional Vortices, and Junction Momentum Exchange in a Partially Covered Submerged Canopy Flume

Xu-Feng Yan[1,2], Huan-Feng Duan[2], Wing-Hong Onyx Wai[2], Chi-Wai Li[2], and Xie-Kang Wang[1]

[1]State Key Laboratory of Hydraulics and Mountain River Engineering, Sichuan University, Chengdu, China, [2]Department of Civil and Environment Engineering, The Hong Kong Polytechnic University, Hong Kong, China

Abstract This study experimentally investigated the influence of a model-submerged canopy on three-dimensional hydrodynamic structures in a partially obstructed flume. Canopy density, water discharge, and water depth were varied to achieve generalized conclusions. With tracer experiments, multi-dimensional (vertical and horizontal) large-scale coherent vortices arising from both the top and lateral edges of the canopy were visualized. The results of the mean flow and turbulence field show that the hydrodynamic characteristics are highly three-dimensional, impacted by canopy density and submergence ratio. Typical shear layers are confirmed by scaled velocity distribution with local characteristic velocity and length scales in both vertical and transverse directions along the canopy edges except for the near-bed region where horizontal vortices are inhibited. Along the canopy edges, the average effect of the vertical coherent vortices overall outweighs that of the horizontal coherent vortices for dense canopies, the ratio of which can be regressed more precisely with the water-related Reynolds number. The vertical profiles of the longitudinal velocity in the near-junction region are characterized by near-bed velocity deflection, strengthened by the increase in canopy density. The negative velocity gradients are found to be more closely related to the drag length-related Reynolds number. An in-depth analysis of secondary flows and near-junction momentum budget has been conducted to show the mass and momentum exchange processes. The results show that multidimensional coherent vortices and turbulence-induced secondary flows play different roles in mass and momentum exchange, accounting for near-bed velocity deflections in the junction region.

1. Introduction

Vegetation frequently grows partially on channel bed (e.g., vegetation colonization on shallow sediment bars and vegetation in drainage channels for ecosystem restoration), creating spatially nonuniform vegetative roughness across the channel bed with different vegetation submergence scenarios. As a result, hydrodynamics are substantially modified, thus impacting the sedimentary processes and morphodynamics of the channels (Jordanova & James, 2003; Kim et al., 2015; Le Bouteiller & Venditti, 2015; Neary et al., 2012; Wang et al., 2018; Xu et al., 2019) and dispersion processes (Guo et al., 2020; Huai et al., 2020; Li & Wang, 2002; Murphy et al., 2007; Rubol et al., 2016; Shucksmith et al., 2011). To date, characteristics of mean flow and turbulence in partially obstructed channels have been explored extensively (Bennett et al., 2002; Caroppi et al., 2019; Chen et al., 2012; Huai et al., 2015, 2019; Meftah et al., 2014; Meftah & Mossa, 2016; Rominger & Nepf, 2011; Su & Li, 2002; Truong et al., 2019; White & Nepf, 2007; Yang et al., 2019). Most existing studies, however, documented depth-averaged two-dimensional hydrodynamics under the assumption of shallow water flow.

Flows in a partially covered channel with a submerged canopy can be transformed into a two-dimensional problem by increasing the canopy width or decreasing the water depth. When the submerged canopy extends fully across the channel bed (canopy width equivalent to channel width, $b = B$; Figure 1a), flow is strongly sheared at the canopy top, leading to large-scale coherent vortices rotating in the vertical plane (hereafter referred to as vertical coherent vortices) triggered by the Kelvin–Helmholtz flow instability (Bao & Li, 2017; Ghisalberti, 2002; Li & Busari, 2019; Zeng & Li, 2014). In this regard, periodic vertical mass and momentum exchanges are driven by the vertical coherent vortices, leading to the hydrodynamic behavior of flow shear layers against the canopy top. When the partially distributed canopy becomes emergent (water depth lower than canopy height, $h > H$; Figure 1b), mass and momentum exchanges are dominant in the horizontal dimension due to the formation of large-scale coherent vortices rotating in the horizontal plane (thereafter referred to as horizontal coherent

Writing – review & editing: Huan-Feng Duan, Wing-Hong Onyx Wai, Chi-Wai Li, Xie-Kang Wang

vortices). Consequently, a shear layer forms against the lateral edge of the canopy. It has been found that those coherent vortices in different dimensions are triggered by flow shearing at canopy edges, which is impacted by canopy density (a) and water depth (H). Nepf (2012) reported that coherent vortices may arise when $aH > 0.1$. For large-scale vortex-driven flows, the profile of the longitudinal velocity approximates a hyperbolic tangent curve with an inflection point occurring at or near the edges of the canopy, coinciding with peaked Reynolds stresses. The scaling of the velocity and Reynolds stress distribution have been investigated by previous studies (Ghisalberti, 2002; Meftah & Mossa, 2016; Meftah et al., 2014; White & Nepf, 2007).

Scaling characterization exists in longitudinal velocity for these two flow and canopy configurations regarding different dimensions. Figure 1c illustrates characteristic velocity and length scales of a longitudinal velocity profile above the submerged canopy described by Ghisalberti (2002). A scaling relationship is given as

$$\frac{\left(U - \overline{U}\right)}{\Delta U} \sim \frac{z - \bar{z}}{t_{ml}/(7.1 \pm 0.4)} \tag{1}$$

where $\Delta U = U_{z2} - U_{z1}$ with U_{z1} and U_{z2} being the minimum and maximum velocities of the mixing layer, respectively; z_1 and z_2 are vertical positions of the lower and upper bounds of the mixing layer; z_1 is at the vertical location where $(U - U_{z1})/\Delta U = 0.01$; z_2 is at the surface; $\overline{U} = (U_{z1} + U_{z2})/2$ at the vertical distance from the bed, $\bar{z} = (z_1 + z_2)/2$, indicating the center location of the mixing layer; $t_{ml} = z_2 - z_1$, is the thickness of the mixing layer. Figure 1d illustrates characteristic velocity and length scales of a longitudinal velocity profile adjacent to an emergent canopy described by White and Nepf (2007). The neighboring outer region bears a scaling between characteristic velocity and length, given as

$$\frac{U - U_m}{U_{y2} - U_m} \sim \frac{y - y_m}{\delta_2} \tag{2}$$

where U_{y1} is the uniform velocity in the inner vegetation region; U_{y2} is the uniform velocity in the outer region; U_b is the velocity at the lateral edge; y_m is the transverse coordinate where the transverse velocity gradient of the inner half matches that of the outer half; U_m is the velocity at y_m. δ_1 is the inner layer length and δ_2 is the outer layer length. However, above two-dimensional hydrodynamics and scaling approaches have not been tested for a partially obstructed channel with a submerged canopy where mean flow and turbulence are three dimensional and anisotropic. Such flow and canopy configurations commonly occur under high flows (e.g., flooding event), deep-narrow drainage channels, or submerged vegetation largely colonizing the channel bed. In this regard, horizontal and lateral interfaces coexist at the top and lateral edges of the canopy, respectively, and multidimensional coherent vortices and turbulence-induced secondary flows may govern more complex processes of mass and momentum exchanges between the canopy region and outer open water body (Nezu & Onitsuka, 2001; Yan et al., 2016).

Only some studies were concerned with three-dimensional mean flow, turbulence, and vortex development in partially obstructed channels in flume experiments (Nezu & Onitsuka, 2001; Devi & Kumar, 2016; D. Liu et al., 2017; Yan et al., 2016). Nezu and Onitsuka (2001) investigated the three-dimensional flow characteristics in a submerged canopy half across the channel bed regarding short canopy ($h = 5$ cm) and shallow water ($H = 7$ cm), and they found the coexistence of multidimensional (vertical and horizontal) coherent vortices and secondary flows driving mass and momentum exchanges in multidimensions and a linear vertical profile of the longitudinal velocity displaying in the near-junction region. Yan et al. (2016), however, reported a different result of the near-junction region for a tall canopy ($h = 15$ cm) and deep water ($H = 25$ cm) that near-bed velocities are deflected and hyperbolic tangent profiles form in far-bed regions. The near-bed velocity deflection in the near-junction region was also observed by Devi and Kumar (2016) and their results further showed that the seepage may enhance the deflection degree. For a tall emergent canopy ($h = 10$ cm) partially covering a transversely tilting bed, D. Liu et al. (2017) also showed the velocity deflection phenomenon in the near-junction region with a velocity contour, strengthened by the increase in canopy density. Yan et al. (2016) explained that the bed might impose a depressive impact on the development of the horizontal coherent vortices in the near-bed region. With this concept, the authors proposed a vortex-based Spalart-Allmaras (SA) turbulence model and successfully reproduced near-bed velocity deflection. The impact of bed on vegetation-induced coherent vortices also occurs in the wake of a circular vegetation patch found by C. Liu et al. (2017). The generated Karman vortex

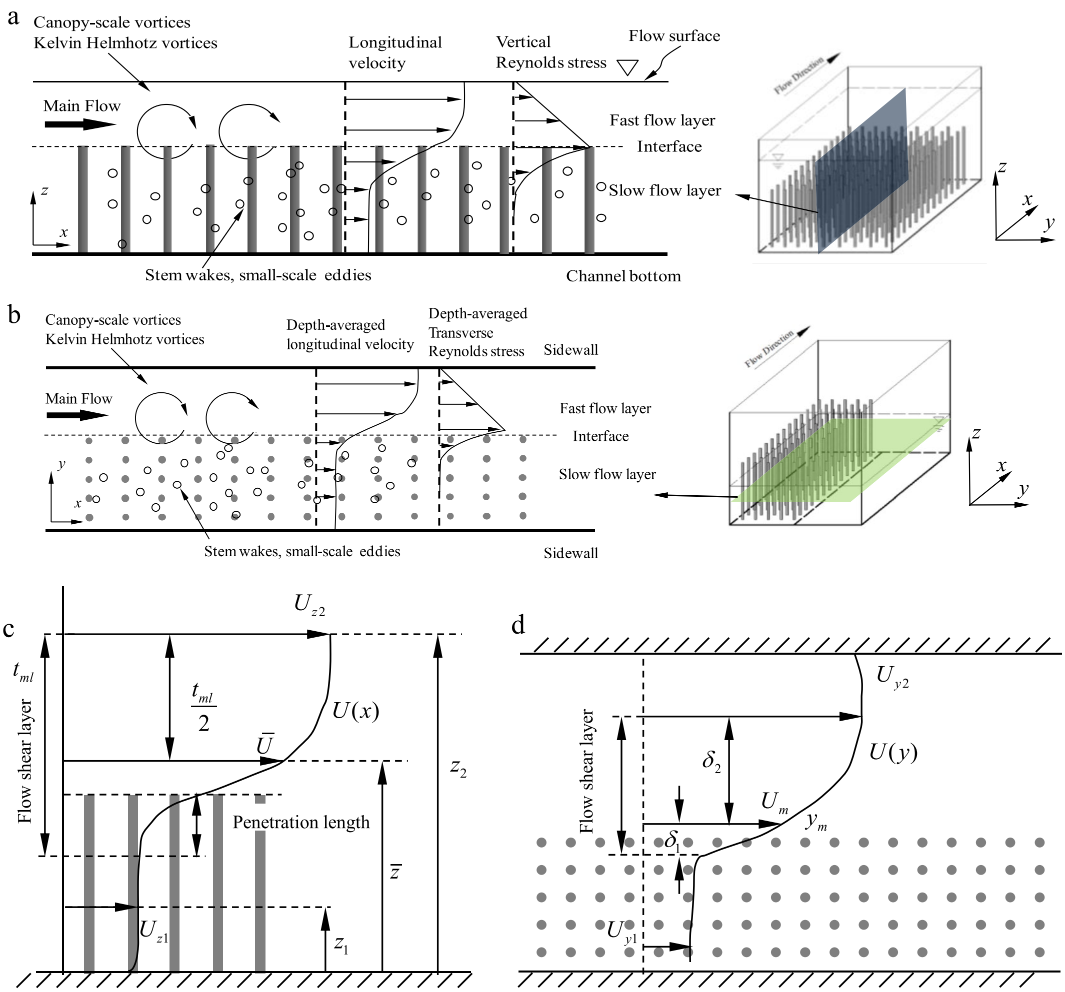

Figure 1. Two-dimensional flow structure in (a) a fully obstructed channel with a submerged canopy, side view and (b) a partially obstructed channel with an emergent canopy, top view. Characteristic velocity and length scales in (c) a fully obstructed channel and (d) a partially obstructed channel.

street cannot be generated under a short vegetation patch. The above studies show that channel bed may play an essential role in impacting the horizontal coherent vortices. Unfortunately, studies have rarely been carried out to explore the underlying physics, which suppresses the understanding of flow behavior in partially obstructed channels with a canopy. With the above arguments, three knowledge gaps can be identified as follows:

1. Rare systematic experimental measurements can offer a picture of three-dimensional hydrodynamics in a partially obstructed channel with a vegetation canopy
2. Existing two-dimensional-based scaling theories for velocity and Reynolds shear stress profiles in vegetated flows have not been examined by three-dimensional flow structure
3. Three-dimensional flow momentum exchange influenced by a submerged vegetation canopy has not been studied, while it is significant for understanding hydrodynamic behaviors in partially obstructed channels

To fill up the above knowledge gaps, this study investigates and understands the three-dimensional hydrodynamic behavior in a channel partially obstructed by a submerged model vegetation canopy with laboratory experimental measurements. The spatial patterns of mean velocity, Reynolds stresses, Turbulent Kinetic Energy (TKE), secondary flows, and multidimensional vortex characteristics are examined. Generalized results are obtained with varying flow and canopy configurations (water discharge, depth, and canopy density). Existing scaling approaches for flow shear layers derived from two-dimensional vegetated flows are tested by three-dimensional experimental data. To strengthen the understanding of mass and momentum exchange processes driven by both multidimensional vortices and secondary flows, a quantitative analysis of the near-junction momentum budget is carried out.

This paper is organized as follows. The flume setup, vegetation configurations, and analytical methods for flow are described in Section 2. The visualization of multidimensional coherent vortices, the patterns of mean flow and turbulence, and the scaling of velocity and Reynolds stresses are presented in Section 3. In Section 4, a discussion section is presented, including how multidimensional coherent vortices are impacted by flow and canopy configurations, near-bed velocity deflection behavior, and interactions between mean flow, secondary flows, and multidimensional coherent vortices. Lastly, conclusions are drawn in Section 5.

2. Experiments and Methods

2.1. Recirculation Flume System

Experiments were carried out in a flume in the Hydraulics Laboratory at The Hong Kong Polytechnic University. The flume has a length, width, and depth of 12.5, 0.31, and 0.4 m, respectively. Its sidewalls are made out of glass and its bottom is made out of steel. The flume bed is set with a fixed slope (S) of 1/300. A honeycomb is installed at the entrance of the flume such that large-scale eddies can be filtered earlier. Water depth is adjusted by the tailgate at the flume exit. Four water tanks are connected to close the entire system. A pump is installed to provide water recirculation. The water discharge (Q) capacity is from 0 to 100 L per hour (l/h) and it is monitored by using a PROMAG type electromagnetic flow meter.

2.2. Vegetation Canopy Geometric Configurations

Solid cylinders are widely used to build model vegetation canopies in vegetated flow studies (Liu et al., 2008; White & Nepf, 2007; Yang et al., 2007, 2015) for their simple geometries and convenience of measurement equipment installation. Figure 2 shows the sketch of the reach of interest, including (a) plan view, (b) side view, (c) cross-section view, (d) stem arrangement, and (e) measurement vertical arrangement. Plastic cylinders of height h = 15 cm and diameter d = 0.5 cm are used to model vegetation stems, which are mounted onto a PVC board with a rectilinear grid pattern. The spacing between adjacent elements in both the longitudinal and transverse directions are 3×3, 6×3, and 6×6 cm, respectively. As a result, three stem number densities (n = 1111, 556, and 278m^{-2}) defined as the number of vegetation elements per unit area are included in flume experiments. The frontal area per unit volume or canopy density (a) is defined as the product of effective width (= cylinder diameter) and stem number density is $a = nd$ = 5.56, 2.78, and 1.39 m^{-1}, respectively. Accordingly, the solid volume fraction is given as $\lambda = \pi ad/4$ = 0.022, 0.011, and 0.005.

The vegetative drag coefficient is a significant parameter, which may influence how we understand the experimental results of hydrodynamics in vegetated flows. Previously, experimental and numerical studies were used to quantify the vegetative drag coefficient. Dunn (1996) based on experimental results proposed a unified value of 1.13 for the averaged drag coefficient. Kothyari et al. (2009) used sensor technology to directly measure the drag coefficient for emergent canopy and proposed formula, $C_d = 1.53[1 + 0.45\ln(1 + 100\lambda)]\mathrm{Re}_d^{-3/50}$, where Re_d represents Reynolds number related to cylinder diameter. According to the formula, C_d is dependent on vegetation density and flow condition. Using the pore velocity concept, Cheng and Nguyen (2011) based on experimental data proposed a theoretical model for drag coefficient, $C_d = 130/r_{v*}^{0.85} + 0.8\left[1 - \exp\left(-r_{v*}/400\right)\right]$, where $r_{v*} = \left(gS/v^2\right)^{1/3} r_v$ and $r_v = \frac{\pi}{4} d(1-\lambda)/\lambda$ for λ = 0.0043–0.1189; Etminan et al. (2017) used highly resolved LES modeling velocity data to develop a new model for drag coefficient with emergent canopy $C_d = 1 + 10\mathrm{Re}_c^{-2/3}$, where $\mathrm{Re}_c = \frac{U_0}{1-\sqrt{2\lambda/\pi}} \frac{d}{v}$ for λ = 0.016–0.25. Except for the sensor approach that overestimates drag coefficients (C_d = 1.16–1.56) for the current canopy-flow configurations, the other three approaches are appropriate to estimate drag coefficient, which is C_d = 0.97–1.21 by Cheng and Nguyen (2011) and C_d = 1.07–1.11 for Etminan et al. (2017). Considering that λ = 0.005–0.022 for this study is relatively close to that for Cheng and Nguyen (2011), drag coefficients are estimated as C_d = 0.97, 1.08, and 1.21 for the employed three canopy densities. Note that C_d = 1.21 for λ = 0.022 can be justified by the model validation in Yan et al. (2016) by adopting C_d = 1.2. Accordingly, the drag length scale $(C_d a)^{-1}$ = 0.15, 0.33, and 0.74.

10.1029/2020WR029494

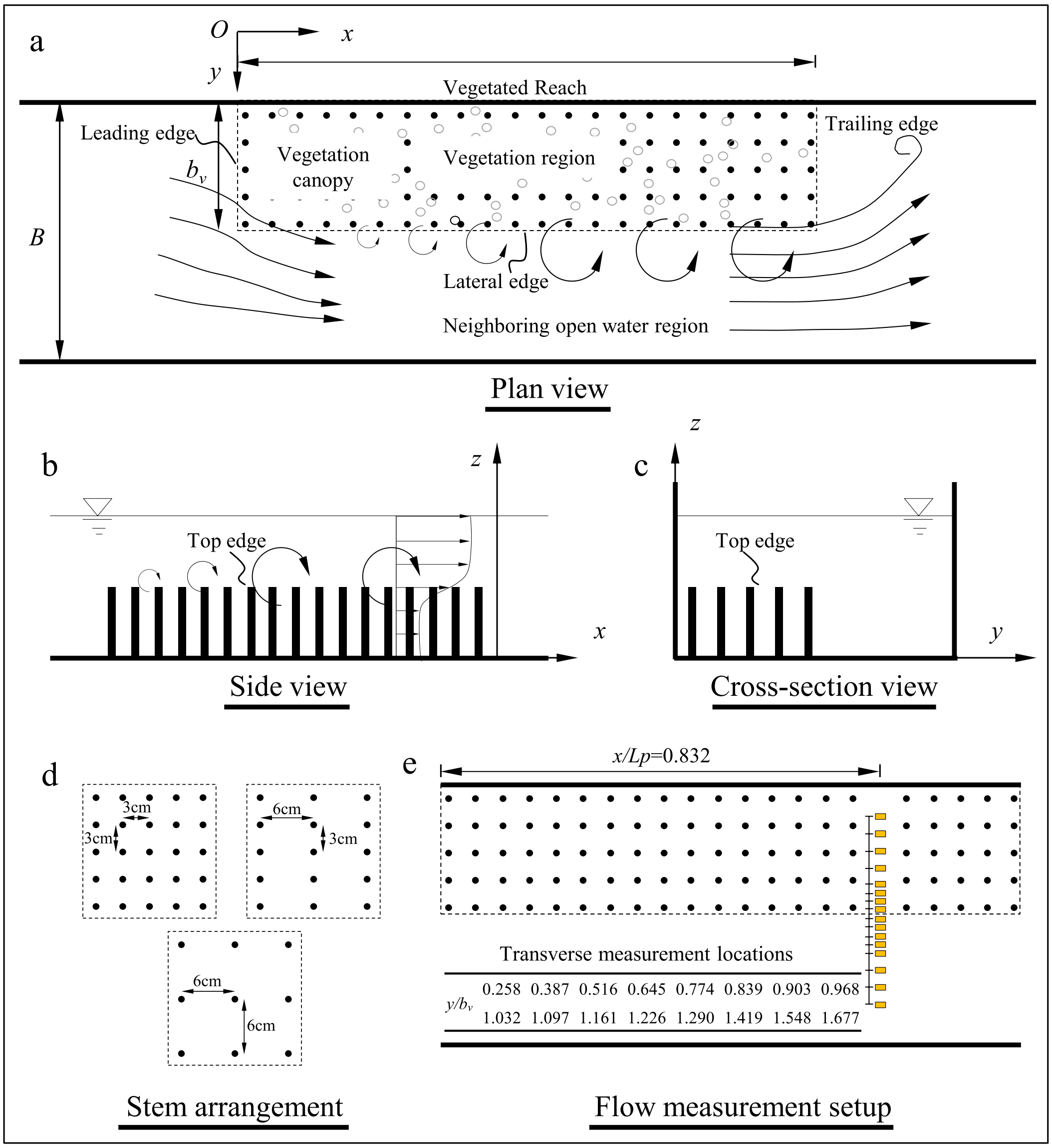

Figure 2. Sketch of the experimental research setup and vegetation canopy configurations. (a) Plan view; (b) side view; (c) front view; (d) tree canopy density definition; and (e) measurement vertical arrangement. The coordinate is $x = 0$ at the leading edge, $y = 0$ at the side wall, and $z = 0$ at the bottom.

2.3. Tracer Visualization Experiments

To show large-scale coherent structures arising from the canopy-water interfaces, the tracer dye visualization is a good means, which has been employed by previous studies on vegetated flows. Zong and Nepf (2011) used red tracer dye to visualize wake vortex structure (associated characteristic length scales) downstream a circular porous cylinder patch. C. Liu et al. (2017) used fluorescein dye excited by ultraviolet light for vortex visualization and length scale analysis. Compared with the above studies where two-dimensional vortex structures exist, large-scale vortices in this study should be three dimensional, which means that coherent vortices may coexist in different dimensions. Therefore, the tracer releasing points were arranged in different spatial locations for a cross section of fully developed flow conditions (details see later). Two cameras with the frame rate ~30 frames per second were installed on one side and above the flume, respectively, to co-film the tracer paths in different dimensions. The dye tracer release tube was placed at $x/Lp = 0.5$, after which dye tracers can move with vortex circulations along the canopy. The sights of two cameras covered a reach of at least $x/Lp = 0.5$–1. The recording duration for all runs ranged from 20 to 30s, which allowed clear observations of at least four vortex cycles (for

10.1029/2020WR029494

cases where vortices were formed). Note that the aim of the tracer experiments is used to visualize the formation of large-scale vortices instead of assessing vortex sizes (or characteristic length scales) like previous studies (Liu et al., 2018; Zong & Nepf, 2011).

2.4. Velocity Measurements and Data Processing

For the three canopy densities, water discharge and depth were varied to achieve various flow configurations. The water discharge (Q) is 40 l/hr ~ 75 l/hr and the canopy was maintained to be submerged with the water depth (H) falling at a range of 0.215–0.302 m. As a result, the flow configurations lead to the mean velocity $U_0 = Q/(BH) = 0.157$ m/s – 0.317 m/s, the ratio of water depth to canopy height $H/h = 1.37$–2.01, and the aspect ratio (channel width/water depth, B/H) = 1.03–1.51. This experiment setup can be found during high flows (e.g., floods), deep-narrow drainage channels, or submerged vegetation colonizing the channel bed (e.g., vegetated ditches). Nepf (2012) suggested that vertical canopy-scale vortices occur for submerged vegetation when $aH > 0.1$. In our experiments, $aH = 0.834$, 0.417, and 0.209 indicates that coherent vortices shall form around the canopy edges according to Nepf's suggestion. Traditionally, Reynolds number with different forms is used to characterize important hydrodynamic properties. For instance, depth-related Reynolds number, particle Reynolds number, and stem Reynolds number are widely employed for the analysis of nonobstructed channel flows and sediment incipient motion on bare beds and vegetated beds (Cheng, 1997; He et al., 2019; Liu & Nepf, 2016). A new Reynolds number should be defined to characterize the partial obstruction configuration. For vegetated flows, the drag length scale ($(C_d a)^{-1}$) has been justified to be an essential parameter to characterize the hydrodynamics. For a partially obstructed channel with a submerged canopy, we can define a cross-sectional drag length scale ($(C_d a)^{-1} bh/BH$), indicating the drag length averaged over the cross-sectional area. This new drag length scale depends on the canopy area positively and the entire cross-sectional area negatively, reflecting that the vegetative drag effect tends to be less significant with a smaller canopy area. For this study, the cross-sectional averaged drag scale mainly depends on the variation of the water depth since the canopy region area is fixed. Therefore, a new Reynolds number based on the cross-sectional averaged drag scale termed drag length-related Reynolds number can be given as $\mathrm{Re}_{DL} = U_0((C_d a)^{-1} bh/BH)/\nu$, where $\nu = 1.01 \times 10^{-6}$ m^2/s is the water kinematic viscosity. Re_{DL} is associated with both mean flow characteristics and the relativity of the canopy to the entire water body. The experimental flow and canopy configurations are summarized in Table 1.

The three-dimensional instantaneous flow velocities (*u, v, and w*) were measured using the latest generation acoustic Doppler velocimetry (ADV), namely Vectrino-II. Different from conventional ADV sensors (e.g., Vectrino and Vectrino Plus) measuring only one point at once, Vectrino-II can provide a profiling region of approximately 40–80 mm in height from the central transducer. The profiling region consists of up to 35 sampling points with an accuracy of 1 mm. Thus, the improvement enables high-resolution measurements of flow velocities with much reduction of time consumption of experiments. The density of sampling points in the profiling region can be configured in Multiple Instrument Data Acquisition System software. Vectrino II has been increasingly employed to investigate surface flow velocities under various geometric configurations (Bao & Li, 2017; Horstman et al., 2018; Risse-Buhl et al., 2017).

Time-averaged flow velocities (U, V, and W) were determined by the measured instantaneous velocities (Equation 3). Two-point velocity correlations referred to as Reynolds stresses and turbulent intensities and TKE were calculated by Equations 4–6.

$$U_i = \frac{1}{T}\int_0^T u_i dt \tag{3}$$

$$-\overline{u_i' u_j'} = \frac{1}{T}\int_0^T (U_i - u_i)(U_j - u_j)\, dt \tag{4}$$

$$\overline{u_i'} = \sqrt{\frac{1}{T}\int_0^T (U_i - u_i)^2 dt} \tag{5}$$

10.1029/2020WR029494

Table 1
Summary of Experimental Runs

Run	Q (l/h)	H (m)	U_0 (m/s)	Re_H	Re_{DL}	N (m^{-2})	$\phi\lambda$	a (m^{-1})	B/H	H/h	$(C_d a)^{-1}$ (m^{-1})	ah
L1	50	0.256	0.175	24,993	15,452	1,111	0.022	5.56	1.21	1.71	0.15	0.83
L2	70	0.234	0.268	19,380	9,590	1,111	0.022	5.56	1.32	1.56	0.15	0.83
L3	75	0.302	0.223	14,505	9,301	1,111	0.022	5.56	1.03	2.01	0.15	0.83
L4	70	0.28	0.224	15,432	11,505	1,111	0.022	5.56	1.11	1.87	0.15	0.83
L5	50	0.265	0.169	16,534	8,606	1,111	0.022	5.56	1.17	1.77	0.15	0.83
L6	60	0.275	0.196	22,523	15,689	1,111	0.022	5.56	1.13	1.83	0.15	0.83
L7	60	0.245	0.219	20,833	12,082	1,111	0.022	5.56	1.27	1.63	0.15	0.83
L8	60	0.215	0.25	22,350	10,792	1,111	0.022	5.56	1.44	1.43	0.15	0.83
L9	40	0.228	0.157	20,576	23,207	1,111	0.022	5.56	1.36	1.52	0.15	0.83
L10	40	0.205	0.175	25,926	34,963	1,111	0.022	5.56	1.51	1.37	0.15	0.83
M1	50	0.251	0.178	23,148	24,097	555	0.011	2.78	1.24	1.67	0.33	0.42
M2	70	0.22	0.285	22,341	61,041	555	0.011	2.78	1.41	1.47	0.33	0.42
M3	70	0.265	0.237	26,065	71,214	555	0.011	2.78	1.17	1.77	0.33	0.42
M4	60	0.25	0.215	29,163	75,728	555	0.011	2.78	1.24	1.67	0.33	0.42
S1	50	0.253	0.177	22,794	9,940	278	0.005	1.39	1.23	1.69	0.74	0.21
S2	70	0.218	0.288	16,896	9,222	278	0.005	1.39	1.42	1.45	0.74	0.21
S3	80	0.226	0.317	17,105	19,186	278	0.005	1.39	1.37	1.51	0.74	0.21
S4	60	0.218	0.247	17,021	37,767	278	0.005	1.39	1.42	1.45	0.74	0.21

Note. Q - water discharge, H - water depth for fully developed flows, U_0 - cross-sectional averaged velocity for fully developed flows, h - canopy height, Re_H - depth-related Reynolds number, a - frontal area per volume, B/H - aspect ratio (width/depth), and H/h – canopy submergence.

$$\mathrm{TKE} = \frac{1}{2}\sum_{i=1}^{i=3}\left(\overline{u_i'^2}\right) \tag{6}$$

In the above equations, the subscript $i = 1$, 2, and 3 represents three dimensions.

As seen in Figure 2e, the measured cross section was selected at $x/L_p = 0.832$, where the flow was fully developed. The longitudinal variation of velocity profiles along the canopy for two water discharges can be referred in Figure S1 in Supporting Information S1. This selected location is also consistent with $0.81L_p$ suggested by Rominger and Nepf (2011). Totally, 16 verticals of measurement were set across the entire channel bed, with a denser arrangement (1 cm interval) in the near-junction region and a sparser arrangement (2 cm interval) in the away-junction region. This enables to capture the rapid transition of the flow shear layer in the junction region. To ensure the capture of high-frequency turbulence, the sampling rate and number were set to 75 Hz and 5,000, respectively, as recommended by Nezu and Nakagawa (1993) and Chanson et al. (2007). Also, an analysis of sampling number and period can be found in Figure S2 in Supporting Information S1, which confirms that the sampling number and period are sufficient to capture mean flow and turbulence information in the current flow and canopy configuration. To refine the quality of the measured data such as high instantaneous velocity spikes, the phase-space thresholding technique developed by Goring and Nikora (2002) was employed. Those instantaneous velocity spikes were first identified by the employed approach and were then replaced by time-averaged velocity or accurate neighboring nonspike data (we used the former). Manipulating the algorithm codes within Matlab2015b, the processed results can be referred to Figures S3S4 in Supporting Information S1. In experiments, the canopy was submerged and various flow configurations were set by varying the flow rate and adjusting the tailgate. The information of flow conditions is summarized in Table 1. For a clear statement, three vegetation densities are considered: Run L1-L10 in Supporting Information S1 for high density ($a = 5.56\ m^{-1}$), Run M1-M4

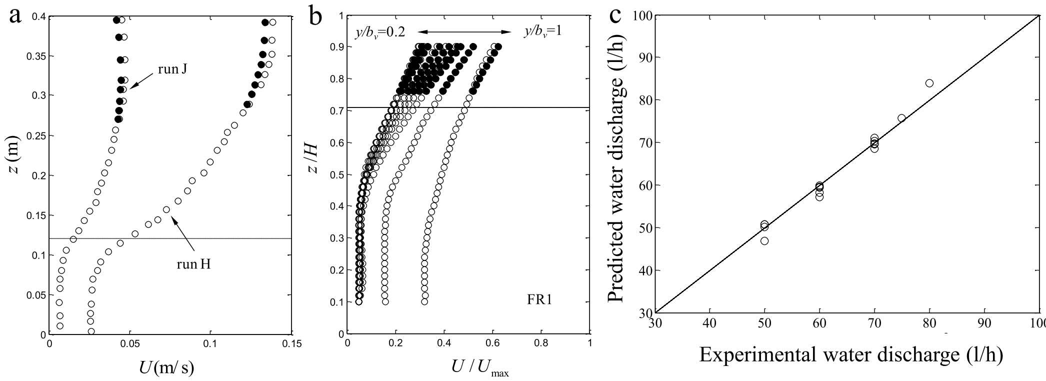

Figure 3. Extrapolation of the longitudinal velocity near the water surface. (a) A fully obstructed channel with a submerged canopy (Ghisalberti & Nepf, 2004); (b) a partially obstructed channel with a submerged canopy (Nezu & Onitsuka, 2001); and (c) comparison between the predicted and experimental water discharges in this study.

in Supporting Information S1 for mediate density ($a = 2.78\ \mathrm{m}^{-1}$), and Run Figures S1-S4 in Supporting Information S1 for low density ($a = 1.39\ \mathrm{m}^{-1}$).

Regions of 4 cm below the water surface are missing (blind) for a down-looking Vectrino II used in the current experimental work. It is desirable to extrapolate velocity information to blind regions below the water surface. To handle this problem, Blanckaert and Graf (2001) used smooth splines to extend measured flow parameters (by ADVP) to blind regions near the water surface in a sharp bend. Physical boundary conditions such as the no-slip condition on solid boundaries and the free-slip condition at the water surface were applied in the extrapolations. Similarly, the missing flow information at the water surface and side-wall regions can be analytically obtained to complement the flow information in the entire cross-section. A comparison is given below to reveal the accuracy of the extrapolations regarding the longitudinal velocity in terms of data from existing literature (see Figures 3a and 3b). The predicted results agree well with the experimental data. By integrating the longitudinal velocity over the cross-section area ($=\int_0^B \int_0^H U\,d z d y$), the water discharge can be estimated. Figure 3d shows a good agreement between the predicted and experimental water discharges in this study.

3. Results

3.1. Formation of Multidimensional Coherent Vortices

In general, large-scale coherent vortices tend to be generated owing to the pronounced canopy shear layer development. For this study, two interfaces exist at the top edge and lateral edge of the canopy. Simple dye tracer release experiments are carried out to visualize the fluctuating large-scale flow motions (coherent vortices) in multidimension. The dye releasing is conducted at $x/Lp = 0.7$, where the flow condition approximates fulldevelopment. Four locations in the cross section around the canopy characterized by typical hydrodynamics are selected for tracer releasing (see Figure 4c). The results are illustrated by the images in different views (side view for vertical vortices and plan view for horizontal vortices; Figure 4a). At location A (canopy top edge in the far-junction region), vertical coherent vortices form as $a = 2.78$–$5.56\ \mathrm{m}^{-1}$ with $ah = 0.42$–0.84, consistent with the suggestion of Nepf (2012) that coherent vortices form when $ah > 0.1$. However, it is not sure whether vertical vortices form or not for low canopy density ($a = 1.39\ \mathrm{m}^{-1}$) since the tracer is only slightly wavy and fuzzy. Based on previous experience on tracer experiments in vegetated flows, the interface can also be slightly wavy and fuzzy even if coherent vortices (Karman Vortex Street) do not form (see tracer experiments in C. Liu et al., 2017). The PSD distribution (Figure 4b) at location A confirms that a significant peak occurs for the large density only. At this location, the horizontal coherent motion does not occur but the dispersion of the dye is stronger for lower densities ($a = 1.39$–$2.78\ \mathrm{m}^{-1}$). At location B, which is near the canopy top corner, multidimensional (vertical and horizontal) coherent vortices cooccur near the canopy corner, which can be visualized by the dye tracers from different views. At location C, which is at the lateral edge but below the top, horizontal coherent vortices take the domination of the turbulent events for $a = 5.56\ \mathrm{m}^{-1}$ and $2.78\ \mathrm{m}^{-1}$(Run L3 and M1 in Supporting Information S1). Horizontal vortices seem not to be formed for $a = 1.39\ \mathrm{m}^{-1}$ (Run Figure S1 in Supporting Information S1), while

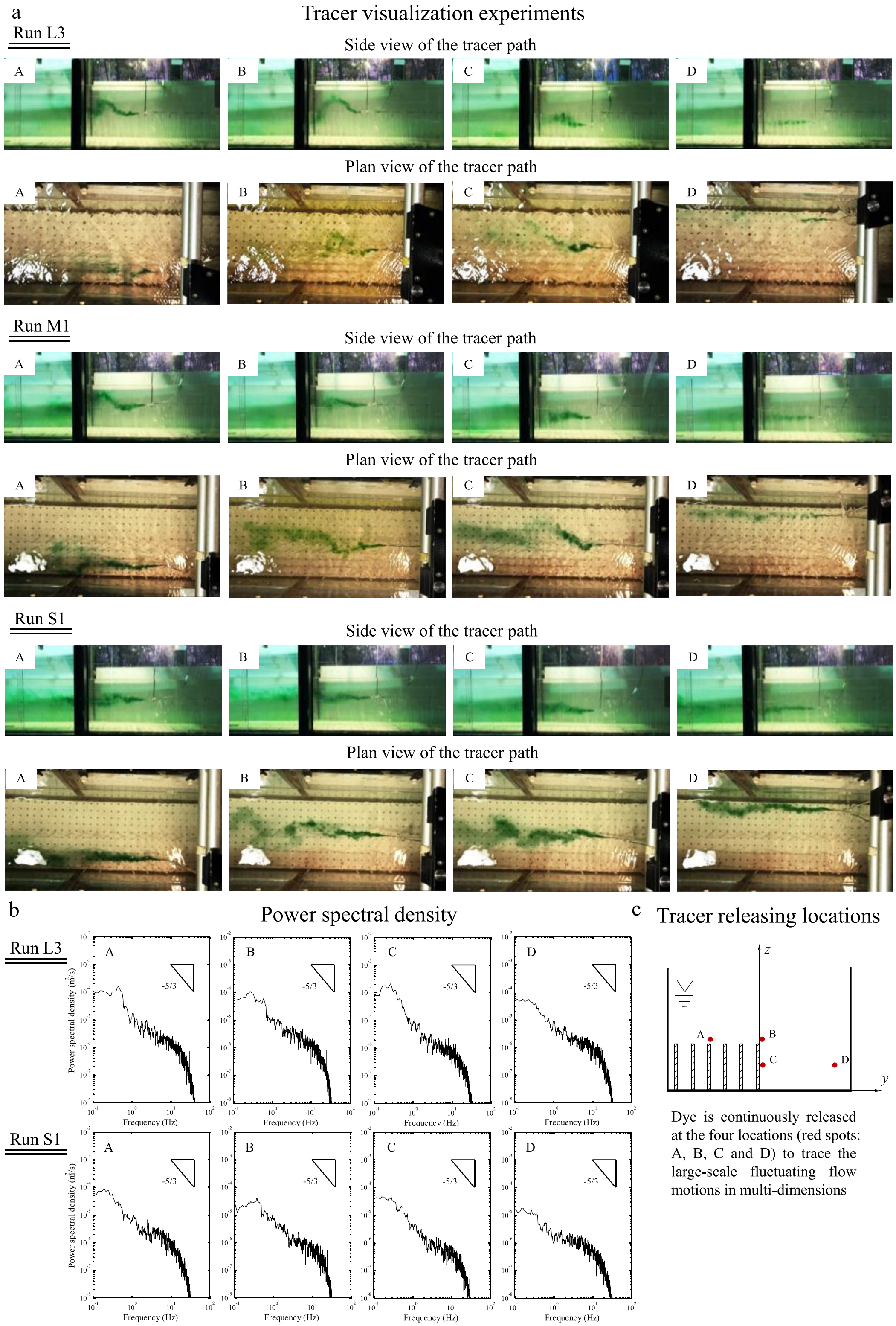

Figure 4. Investigations of large-scale fluctuating flow motions in multidimensions using (a) tracer visualization experiments and (b) power spectral density distribution; and (c) four locations selected to release the dye tracer. The investigated runs include Run L3 in Supporting Information S1 ($a = 5.56$ m^{-1}), Run M1 in Supporting Information S1 ($a = 2.78$ m^{-1}), and Run S1 in Supporting Information S1 ($a = 1.39$ m^{-1}).

turbulent dispersion is still strong for a sparse canopy. At location C, vertical coherent vortices only occur for the highest density ($a = 5.56\ \mathrm{m}^{-1}$) but shrink greatly in terms of vortex size, indicating that vertical coherent vortices can penetrate into the lower layer when vegetation stems disappear. At location D, which is in the far-junction outer open region, no large-scale vortices form for all runs.

The dye tracer visualization results can be also confirmed by the power spectral density (PSD), which is derived by the Fast Fourier transform of the longitudinal velocity (Figure 4b). The results for a high canopy density (Run L3 in Supporting Information S1, $a = 5.56\ \mathrm{m}^{-1}$) and low canopy density (Run Figure S3 in Supporting Information S1, $a = 1.39\ \mathrm{m}^{-1}$) are presented. With the decrease in canopy density, the overall magnitude of the PSD performs a decrease across various scales in turbulence. Magnitude peaks of low frequency (0.1–0.3 Hz) occur in the PSD for locations around the canopy edges (location A, B, and C) for high density (Run L3 in Supporting Information S1), confirming the formation of the multidimensional coherent vortices as visualized by dye tracer experiments (see Figure 4a). The frequency of those peaks is slightly smaller than 0.4 Hz observed by Nezu and Onitsuka (2001) in a large-aspect ratio channel with a shallow water depth. Relatively small magnitude peaks of low frequency only occur at Locations A and B for the low density, indicating the formation of extremely weak vertical coherent vortices. This is also consistent with the dye tracer experimental results.

3.2. Patterns of Mean Velocity, Reynolds Shear Stresses, and Turbulent Kinetic Energy (TKE)

Figure 5 shows the spatial patterns of the longitudinal velocity, Reynolds stresses, and TKE subsequently from left to the right. The analysis and comparison include six runs (L1, M1, S1, L2, M2, and S2 in Supporting Information S1) which are under three canopy densities ($a = 5.56$, 2.78, and $1.39\ \mathrm{m}^{-1}$) and two close flow configurations ($Q = 50$ l/hr and 70 l/hr and $H/h = 1.67$–1.71 and 1.45–1.56).

The spatial patterns of the longitudinal velocity (U) for different runs are illustrated in Figure 5a. Due to the partial obstruction of the submerged canopy, a small velocity zone occurs deep inside the canopy and large velocities occur in the outer water region. The difference between the lowest and highest velocities is promoted by the increase in canopy density. Two zones characterized by high velocity gradients in the vertical and transverse directions link the in-canopy small velocity and outer-water large velocity, indicating canopy shear layer behavior near the canopy edges. Interestingly, isoline bulges pointing the canopy side occur in the near-bed region, which extend transversely outward the open region. These isoline bulges near the bed indicate greater velocity occurs in the lower layer. Furthermore, high canopy density promotes the degree of velocity bulging, and under a small density (S1 and S2 in Supporting Information S1, $a = 1.39\ \mathrm{m}^{-1}$), these bulges become weak or even vanish. Similar velocity bulging shown by the velocity isolines can be found in D. Liu et al. (2017) for an emergent canopy with $H = h = 10$ cm. However, Nezu and Onitsuka (2001) on a submerged canopy with $H = 7$ cm and $h = 5$ cm does not find the velocity bulging probably due to the shallowness effect. Moreover, with a larger canopy density, the near-surface maximum velocity core tends to shift outward the nonvegetated side, suggesting discharge partitioning in a partially obstructed channel substantially impacted by canopy denseness. Choi and Kang (2016) reported that the maximum velocity core over a full obstruction tends to shift toward the side wall with the increase in canopy density. Despite the difference in canopy configuration regarding this and Choi and Kang's studies, the underlying cause might be identical. A simple interpretation can be given: the increase in canopy density tends to enhance the vertical coherent vortices which act as resistance force, which leads to so the maximum velocity core further shifts toward the side wall.

The spatial patterns of vertical and transverse Reynolds shear stresses ($-\overline{u'w'}$ and $-\overline{u'v'}$) are illustrated in Figures 5b and 5c. The two turbulent properties are peaked at the top and lateral edges of the canopy, respectively, which are greater for larger canopy density and cross-sectional mean velocity. For $-\overline{u'w'}$ (Figure 5b), the pronounced cores occur at $y/b \approx 0.70$–0.75 except for Run S2 in Supporting Information S1 (small density) at $y/b \approx 0.95$, indicating the most significant flow shearing in the vertical dimension. The high-value cores extend outward and downward the neighboring open water, and this effect is stronger for higher canopy density. This indicates that high vertical Reynolds stress might be produced or transported into the neighboring open water probably attributed to horizontal coherent vortices or secondary flow motions. For $-\overline{u'w'}$ (Figure 5c), the peak zone of transverse Reynolds stress slightly shifts to $y/b = 1.15$–1.20 rather than just coincide with the lateral edge ($y/b = 1$; Nezu & Onitsuka, 2001; White & Nepf, 2007). Meftah et al. (2014) reported a similar shift of the transverse Reynolds stress at $y/b = 1.20$ and explained that the formation of transversal velocity might be the cause.

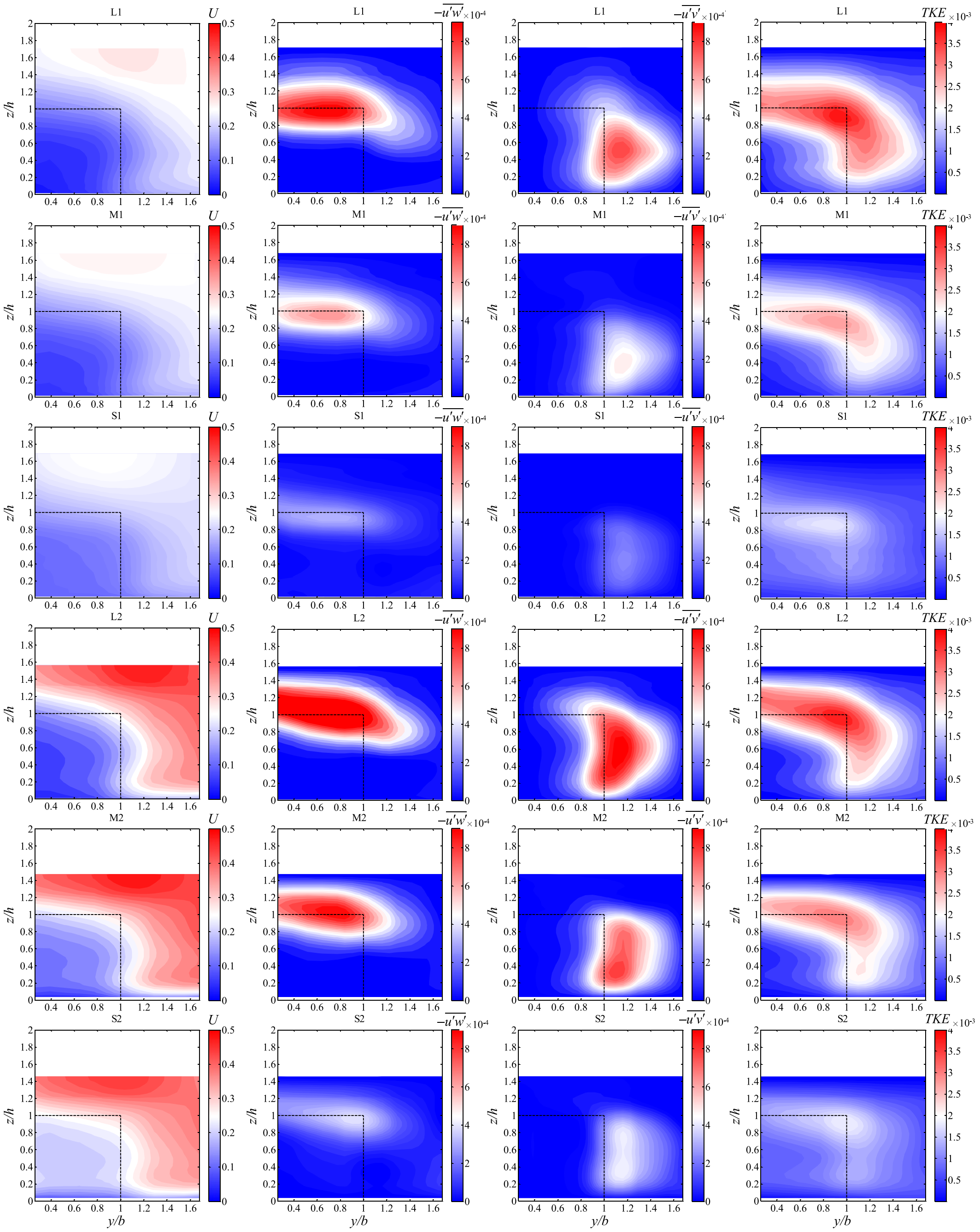

(a) Longitudinal velocity U (m)

(b) Vertical Reynolds stress $-\overline{u'w'}$ (m^2/s^2)

(c) Transverse Reynolds stress $-\overline{u'w'}$ (m^2/s^2)

(d) Kinetic turbulent energy TKE (m^2/s^2)

Figure 5. Spatial patterns of longitudinal velocity, Reynolds shear stresses, and kinetic turbulent energy for runs: L1 and L2 in Supporting Information S1 (U_0 = 0.175 and 0.268 m/s, H/h = 1.71 and 1.56, and a = 5.56 m^{-1}); M1 and M2 in Supporting Information S1 (U_0 = 0.178 and 0.285 m/s, H/h = 1.67 and 1.47, and a = 2.78 m^{-1}); and S1 and S2 in Supporting Information S1 (U_0 = 0.177 and 0.288 m/s, H/h = 1.69 and 1.45, and a = 1.39 m^{-1}).

The peak transverse Reynolds stress nearly centers the lateral edge for all runs and significantly decreases near the bed, indicating the inhibition effect of the bed on the horizontal vortices. Furthermore, the transverse Reynolds stress slightly extends upward of the overflow layer. However, the extension degree is overall much lower when compared with the vertical Reynolds stress extending outward of the open region. This might be because the upper open water body plays a role in stabilizing horizontal coherent vortices, which is similar to the bed effect.

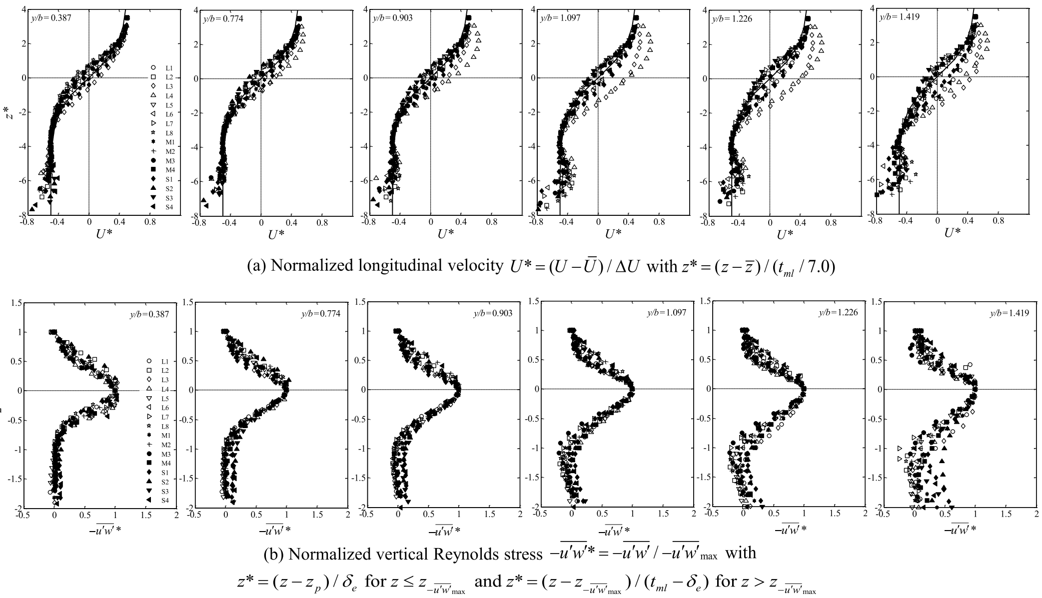

Figure 6. Vertical distribution of scaled (a) longitudinal velocity and (b) vertical Reynolds shear stress at different transverses. For the longitudinal velocity, $U^* = \left(U - \overline{U}\right) / \Delta U$ and $z^* = (z - \bar{z}) / (t_{ml}/7.0)$, described by Equation 1. The solid line indicates a tangent hyperbolic scaling formula, $U^* = 1/2\tanh(z^*/2)$, suggested by Ghisalberti and Nepf (2002). For the vertical Reynolds shear stress, $z^* = \left(z - z_p\right) / \delta_e$ for $z \le z_{-\overline{u'w'}_{\max}}$ and $z^* = \left(z - z_{-\overline{u'w'}_{\max}}\right) / (t_{ml} - \delta_e)$ for $z > z_{-\overline{u'w'}_{\max}}$. $-\overline{u'w'}_{\max}$ is the vertical maximum Reynolds shear stress and $z_{-\overline{u'w'}_{\max}}$ is the vertical position of $-\overline{u'w'}_{\max}$. The solid line indicates the canopy top level.

Figure 5d illustrates the spatial patterns of TKE. The pronounced zone of TKE occurs around the canopy edges as expected, which overall decreases with the decrease in canopy density. The global maximum of TKE occurs near the canopy top corner (i.e., $y/b = 1$ and $z/h = 1$) due to the coexistence of multidimensional (vertical and horizontal) coherent vortices. Interestingly, the decrease in canopy density leads to an apparent reduction of TKE along the lateral edge in the lower layer ($z/h < 0.5$). This behavior, however, is weak for the top edge. As canopy density decreases, the TKE deeply inside the canopy seems to increase, which is related to small eddies shedding off stems promoted by lower canopy densities. Similar results have been reported by previous studies (Nepf & Vivoni, 2000; Poggi et al., 2004).

3.3. Scaling Characterization

The scaling characterization in longitudinal velocity and Reynolds stresses are fundamental for vegetated flows due to the formation of canopy shear layers. Relevant knowledge has been reported in fully obstructed channels with submerged canopy and partially obstructed channels with emergent canopy (Ghisalberti, 2002; White & Nepf, 2007). Our results show that canopy shear layers form around the canopy edges in multidimensions. Herein, scaling approaches arising from the above two-dimensional vegetated flows are examined with the experimental data achieved in the current three-dimensional flows. Since the shear layer widths are not uniform along the canopy edges (see Figures 5b and 5c, Reynolds stress distribution), characteristic velocity and length scales for local verticals, or layers instead of universal values are used for scaling analysis.

Figure 6a presents the results of scaled longitudinal velocity at different transverses. For the verticals of $y/b = 0.387$–0.774, the scaled longitudinal velocities for all runs collapse around a typical tangent hyperbolic curve derived by Equation 1. For $y/b = 0.903$–1.419, the scaling with Equation 1 is still valid for most runs, but more scatters deviate from the standard scaling equation when in the far-junction region (i.e., $y/b = 1.226$–1.419). Despite the deviation, this observation suggests that the standard scaling equation (Equation 1) may still be valid, indicating that the vertical canopy shear layer, to some degree, can extend outward the open water region. However, for $y/b = 1.097$–1.419, the scaled velocities for all runs near $z^* = -6 \sim -4$ systematically deviate from the lower half of the hyperbolic tangent curve. These deviated data well correspond to near-bed velocity

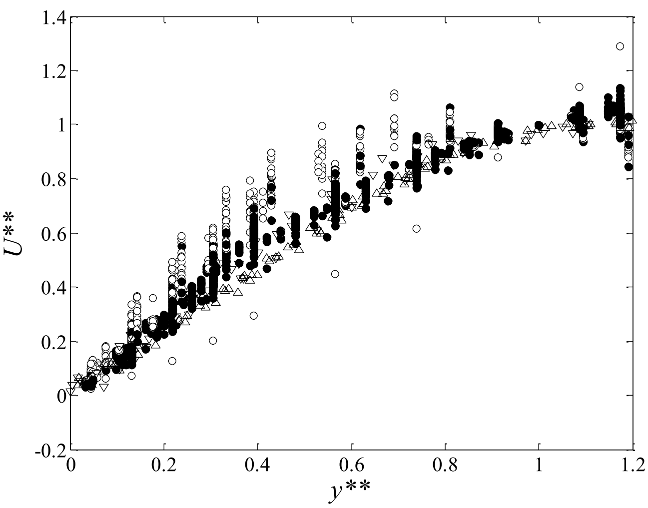

Figure 7. Transverse distribution of scaled longitudinal velocity in the neighboring open water region ($y/b > 1$), described by Equation 2. The symbols are ○, $z/h < 0.29$ and ●, $z/h < 1.0$ for data of the current study; △, Runs (R1–R4 in Supporting Information S1) of Meftah et al. (2014); ▽, Runs (I, IV, VI, and VII) of White and Nepf (2007). $y^{**} = (y - y_m)/\delta_{oy}$ and $U^{**} = \left(U - U_{ym}\right) / \left(U_{y2} - U_{ym}\right)$.

deflection in the junction region, consistent with near-bed velocity bulging displayed in velocity contours (Figure 5a). Therefore, the scaling of the longitudinal velocity in the junction region (open region side) should be limited to the upper flow shear layer if a near-bed velocity-deflection layer exists.

Similar to the longitudinal velocity, the similarity regarding the vertical Reynolds stress can be evaluated. It has been observed that the position of the peaked vertical Reynolds stress ($z_{-\overline{u'w'}_{\max}}$) tends to move down for the nonvegetated side. Herein, $z_{-\overline{u'w'}_{\max}}$ is taken as a reference scaling parameter rather than canopy top level ($z = h$) for the neighboring open water region. Figure 6b presents the scaled vertical Reynolds stress for all runs at different transverse locations. The vertical Reynolds stress is scaled well with the chosen two parameters ($-\overline{u'w'}$ and $z_{-\overline{u'w'}_{\max}}$). Given different runs, the data points almost collapse into a curve, which is typically observed over a submerged canopy fully covering the bed. In the junction region, small observable scattering can be observed below the canopy top level (e.g., $z^* < -0.5$). However, the result is acceptable when $y/b \le 1.226$.

For the transverse distribution, the flow mixing process should occur for the regions below the canopy top due to the development of transverse canopy shear layer. For the region above the canopy top, flow shearing significantly decays, which is indicated by a significant decrease in transverse Reynolds stress (see Figure 5c). Hence, the scaling analysis is only limited to the region below the canopy top. To make a comparison, the experimental data of White and Nepf (2007) and Meftah et al. (2014) are used. Note that the data in this study are three dimensional, so the transverse velocity profiles are plotted regarding different layers over the depth. Figure 7 shows that with scaling manipulation (Equation 2), most of the dimensionless velocities in the outer layer nicely collapse into a tangent hyperbolic curve. However, the velocities in the near-bed region ($z/h < 0.29$) tend to deviate from the resemble curve, which is characterized by a rapid increase near the junction. This behavior of the near-bed velocities indicates that the transverse flow mixing in the near-bed region is much weaker than that in upper regions ($0.29 < z/h < 1$), which can be indicated by the pattern of the transverse Reynolds stress (see Figure 5). This finding is important because some mathematical models (e.g., SA model) assume that the turbulence length scale equal to the distance to the nearest wall is not reasonable when roughness is pronounced (Zeng & Li, 2012). The division definition of the turbulence length scale based on the turbulence field should be more promising (Yan et al., 2016).

4. Discussion

4.1. Dominance of Multidimensional Coherent Vortices

The most predominant hydrodynamic processes in a partially obstructed channel with a submerged canopy are multidimensional coherent vortices arising from the top and lateral edges of the canopy, which have been reflected by tracer visualization experiments, energy spectral density distribution, velocity profiles, Reynolds stresses, and (TKE; see Figures 4 and Figure 5). It is reasonably hypothesized that a synthesis effect of flow condition and canopy configuration can lead to coherent vortices in a particular dimension outweighing the other, which determines the spatial characteristics of the flow mixing process. Two particular scenarios can be easily concluded: only vertical coherent vortices occur near the top edge of the canopy for submerged vegetation fully across the bed and only transverse coherent vortices occur near the lateral edge of the canopy for emergent vegetation partially across the bed. The coevolution of vertical reattached vortices and horizontal Karman vortices shedding from a circular vegetation patch has been reported by C. Liu et al. (2017). The authors argued that the dominant mixing process might be determined by the larger vortex length scale of multidimensional coherent vortices. A straightforward approach to evaluate the dominance of coherent vortices is to calculate the ratio of the average Reynolds stresses at the two edges. Compared with the TKE, the large value of Reynolds stress directly reflects the coherence of velocity fluctuations. Note that peaked vertical and transverse Reynolds stresses occur at the top and lateral edges of the canopy (see Figure 5). It is simple to integrate the maximum Reynolds stresses over the canopy edges and then calculate averaged values over canopy edge widths, which is called edge-width-averaged

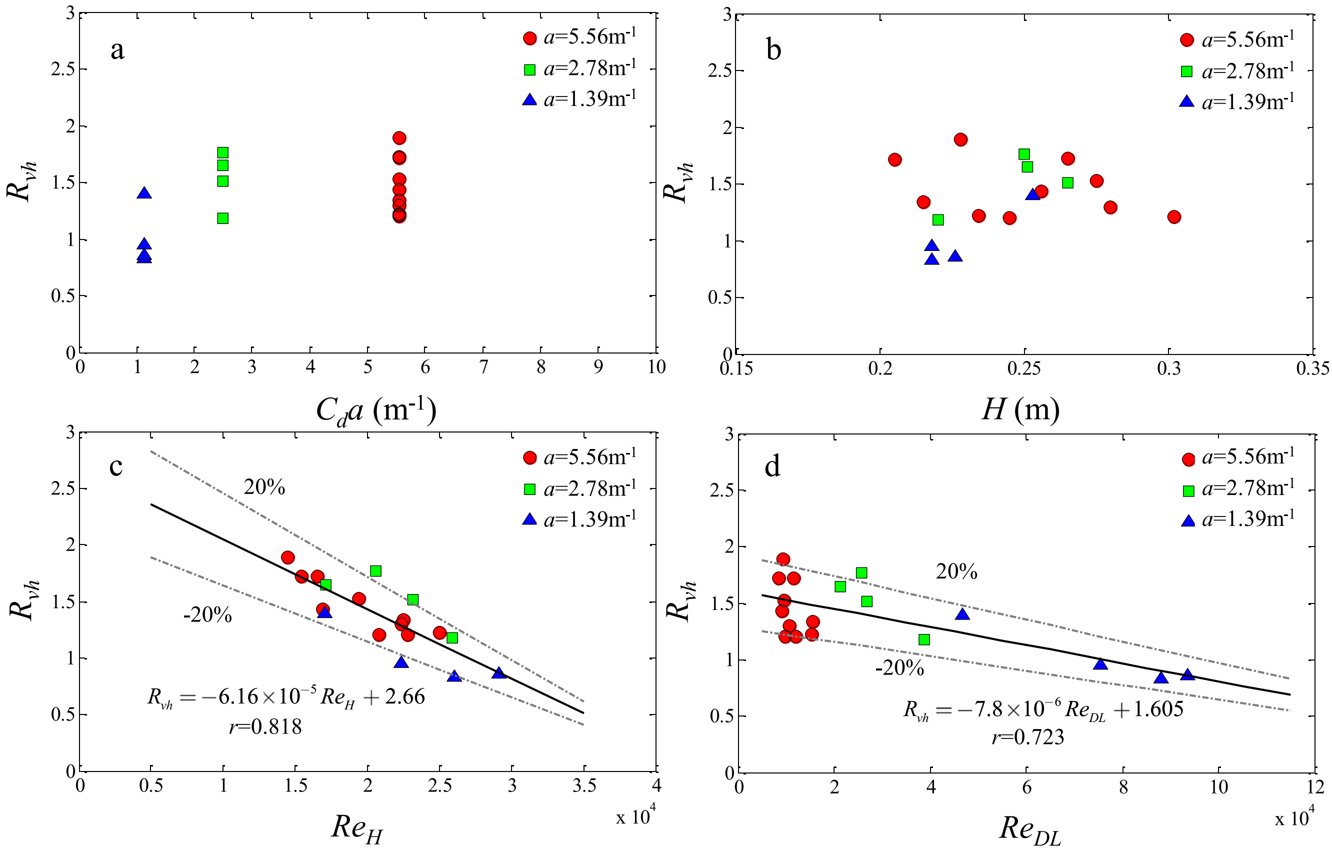

Figure 8. Ratio of the width-averaged vertical Reynolds shear stress to horizontal Reynolds shear stress.

Reynolds stress. Therefore, the ratio of the edge-width-averaged vertical Reynolds stress to the transverse Reynolds stress is given as

$$R_{vh} = \frac{\frac{1}{b}\int_0^b -\overline{u'w'}_{\max} dy}{\frac{1}{h}\int_0^h -\overline{u'v'}_{\max} dz} \tag{7}$$

Figure 8 shows the ratio of the edge-width-averaged vertical Reynolds stress to horizontal Reynolds stress calculated by Equation 7 with different characteristic parameters. In general, the vertical vortices for large canopy density (a = 2.78 and 5.56 m^{-1}) dominate the flow mixing process with the indication of R_{vh} = 1.2–2 (Figure 8a). For a sparse canopy (a = 1.39 m^{-1}), the horizontal coherent vortices might become more significant. Our results suggest that the increase in density might impact the multidimensional coherent vortices to a different degree. For a larger density (a = 5.56 m^{-1}), the water depth (H) does not seem to be a key factor to determine the dominance of coherent vortices (Figure 8b). However, for a smaller density (a = 1.39 and 2.78 m^{-1}), the increase in water depth can enhance vertical coherent vortices more than transverse coherent vortices. This is because the increasing water body of the upper-layer flow tends to play a role in stabilizing horizontal coherent vortices below the canopy top. A similar suppression effect of the increasing height of the overflow layer on the Karman vortex shedding around a circular patch has been reported by C. Liu et al. (2017).

It should be noted that there are no universal quantitatively good relationships between the drag length (C_da) and the ratio (R_{vh}) and between the water depth (H) and the ratio (R_{vh}). However, R_{vh} tends to quantitatively correlate with the Reynolds number in different forms. As shown in Figure 8c,d, a negatively linear curve can regress R_{vh} with the water-depth-related Reynolds number (Re_H) with a relatively high correlation coefficient (r = 0.818). This indicates that a higher inertial force of the fluid (for higher Re_H) can lead to a lower R_{vh}. Therefore, it can be said that a higher mean velocity and a lower water depth both enhance the effect of the horizontal coherent vortices. Another negatively linear curve can also regress R_{vh} with the drag-length-related Reynolds number (Re_{DL})

but with a lower correlation coefficient ($r = 0.723$). Interestingly, the regression using Re_H is better for the higher canopy density ($a = 5.56\ \mathrm{m}^{-1}$) and using Re_{DL} is better for the lower canopy density ($a = 1.39\ \mathrm{m}^{-1}$). However, the reason for the above performance of the regression is not clear, which demands more experiment configurations for a further understanding.

4.2. Near-Bed Velocity Deflection in the Junction Region

Within a submerged canopy, shear layer flows resemble against the top edge of the canopy, represented by hyperbolic tangent velocity profile with an inflection point at the top edge. When the submerged canopy partially covers the channel bed, the shear layer flow theory is still applicable on the vegetated side according to our results (see Figures 6 and Figure 7), suggesting that the presence of the neighboring open water body weakly impacts the flow on the vegetated side. When vegetation stems disappear, the behavior of the vertical canopy shear layer persists over a transverse distance probably due to the formation of vertical coherent vortices, which greatly differs from horizontal canopy shear layer decaying above the canopy top. Of significance is that our results found the occurrence of velocity deflection in the near-bed region originating from the lateral edge of the canopy to the outer zone (Figure 6). This hydrodynamic phenomenon nearly occurs for all runs regarding different canopy densities but with the difference in deflection degree. The junction near-bed velocity deflection phenomenon in a partially obstructed channel with a submerged canopy has been reported by Yan et al. (2016) and Devi and Kumar (2016). Yan et al. (2016) gave a qualitatively descriptive explanation of the formation mechanism: the bed bottom suppresses the formation of the transverse coherent vortices and thus the transverse mixing process, while the developed horizontal coherent vortices far above the bed tend to promote the transverse mixing process. Hence, the nonuniformity of horizontal coherent vortices in the vertical direction lead to the velocity deflection as a result. However, this hypothesis needs the justification of a more detailed quantitative analysis (e.g., momentum flux analysis).

Deflections of the longitudinal velocity are commonly found in various open water flows. The most prevailing one is the surface velocity decrease in large aspect-ratio straight channels referred to as the velocity dip (Nezu & Nakagawa, 1993; Yang et al., 2004). The velocity dip is induced by the formation of secondary flows arising from turbulence anisotropy. Similarly, a parabolic vertical velocity profile can be observed in meandering bends (Blanckaert & Graf, 2001) and downstream junction channel (Li & Zeng, 2009) attributed to the centrifugal force arising from highly asymmetric channel geometry.

Figure 9a shows vertical profiles of the longitudinal velocity at $y/b_v = 1.01$–1.16 for Run L1 in Supporting Information S1 as an example. Several characteristics can be clearly observed within the velocity profile. From the bottom, the velocity increases consistent with the no-slip boundary to a local maximum magnitude U_1 at $z = h_1$. Then, the velocity starts to decrease to another velocity magnitude U_2 at $z = h_2$ over a vertical distance ($h_2 - h_1$). Above $z = h_1$, the velocity profile complies with shear layer flow behavior again. Assume a linear distribution, the negative gradient of the velocity deflection can be estimated as $(U_1 - U_2)/(h_1 - h_2)$.

We plot those negative gradients in different transverse locations against the water-depth-related Reynolds number (Re_H) and drag-length-related Reynolds number (Re_{DL}; Figures 9b and 9c). It can be found that the negative velocity gradients fall in the range from -0.3 to -1.75. The negative velocity gradient increases (smaller magnitude) with the increase in Re_H and $\mathrm{R}e_{DL}$. The drag-length-related Reynolds number (Re_{DL}) is more proper for the description of the negative gradient. The experimental data can be regressed by a logarithmic function with the correlation coefficient ($r = 0.725$), which is much larger than that ($r = 0.605$) for the water-depth-related Reynolds number (Re_H). This suggests that the negative gradient depends more on canopy density than merely flow condition. The negative gradients in Devi and Kumar (2016) (with $a = 4\ \mathrm{m}^{-1}$ and $\mathrm{Re}_{DL} = 7{,}640$) are -0.775 for the nonseepage bed and -1.33 for the 20%-seepage bed, respectively. For such flow and canopy configuration, the negative gradient is estimated -1.38 with the regression relation regarding Re_{DL}.

4.3. Turbulence Anisotropy, Secondary Flows, Momentum Exchange, and Interactions With Mean Flow

The anisotropy in turbulence is a substantial factor to determine mean flow and turbulence field in a partially obstructed channel with a submerged canopy due to the coevolution of multidimensional (vertical and horizontal) coherent vortices. Besides that, turbulence anisotropy also occurs due to the spatially nonuniform distribution of unidimensional vortices such as the bed tending to inhibit horizontal coherent vortices. Thereby, mass and

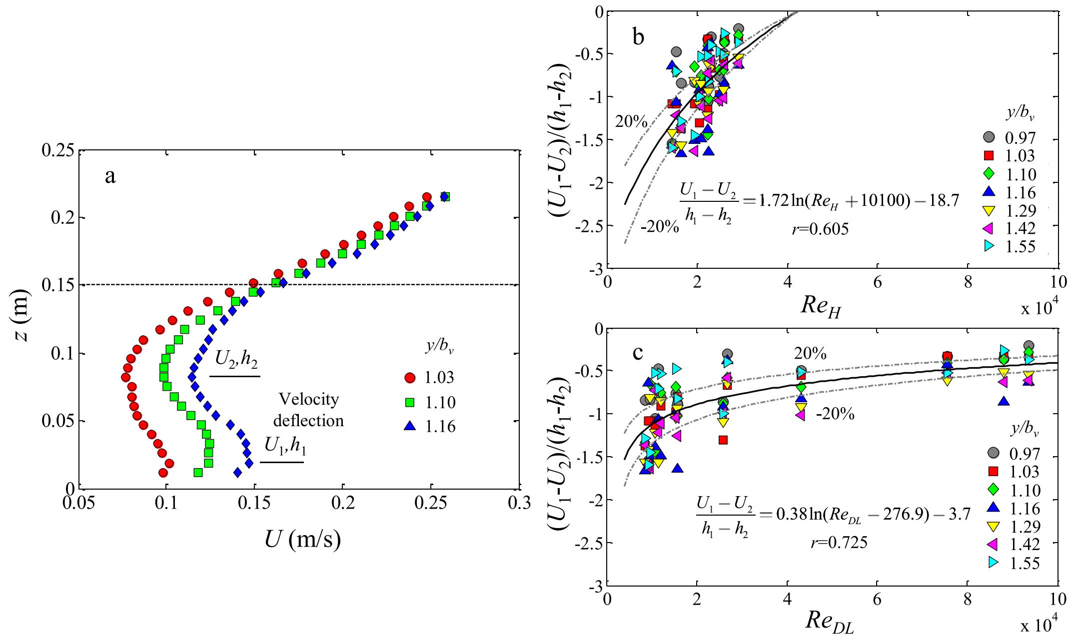

Figure 9. (a) Near-bed velocity deflection in the near-junction region for Run L1 in Supporting Information S1. Negative velocity gradients $\left[(U_1 - U_2)\,/\,(h_1 - h_2)\right]$ due to velocity deflection plotted with (b) water-depth-related Reynolds number, Re_H, and (c) drag-length-related Reynolds number, Re_{DL}.

momentum exchanges are driven by not only large-scale coherent vortices but also likely turbulence anisotropy caused secondary flows. Nezu and Onitsuka (2001) experimentally showed that secondary flows form in a partially obstructed channel with a shallowly submerged canopy ($H = 7$ cm, $h = 5$ cm, $H/h = 1.4$, and aspect ratio = 5.71). For the same flume configuration, Choi and Kang (2006) through numerical modeling showed that the intensity of secondary flows was mediated by the canopy density. It should be noted that compared with the above studies, the canopy height ($h = 15$ cm) and water depth ($H = 22.3$–30.2 cm) for this study are much greater so that the bottom resistance effect for the entire water body should be less significant.

Theoretically, turbulence anisotropy is caused by the fluctuation difference in different dimensions. Although turbulence anisotropy can be indicated by the spatial pattern of Reynolds shear stresses (for example, on the vegetated side but far away from the junction, the vertical Reynolds shear stress dominates near the canopy top), the turbulence anisotropy may still be unclear in some space where vertical and transverse Reynolds shear stresses are both significant. Herein, the characteristics of turbulence anisotropy in a simple way can be quantitatively evaluated by the difference in vertical and transverse components of Reynolds shear stresses, that is, $\overline{u'w'} - \overline{u'v'}$. Figures 10a and 10b illustrates the spatial pattern of $\overline{u'w'} - \overline{u'v'}$ and flow fields of V-W vectors for different canopy densities. It can be clearly observed that turbulence anisotropy shows a similar pattern under the variation of vegetation density. Specifically, two sources of turbulence anisotropy characterized by opposite signs are formed against the canopy (top and lateral) edges but the anisotropic effect becomes less for the small density. The negative anisotropic zone ($\overline{u'w'} - \overline{u'v'} < 0$) along the canopy top edge and positive anisotropic zone ($\overline{u'w'} - \overline{u'v'} > 0$) along the canopy lateral edge indicate the domination of the vertical and transverse coherent vortices, respectively. However, the spatial pattern differs slightly from the spatial distribution of Reynolds shear stresses (see Figure 5). This is because turbulence anisotropy is offset by opposite components in some space. In this sense, the turbulence anisotropy effect diminishes near the canopy top corner, which means that the turbulent effect induced by both vertical and transverse dimensions is equivalent even though the resultant turbulence (as indicated by the peaked TKE) attains the maximum (see Figure 5).

Under a large vegetation density (e.g., Run L1 and Run L3 in Supporting Information S1), two clockwise circulation cells occur in the junction region below and above the canopy top, which is fairly consistent with the spatial pattern of turbulence anisotropy. It appears that the other two anticlockwise circulation cells are formed beside junction circulation cells. In the case of small vegetation density (e.g., Run S1 in Supporting Information S1),

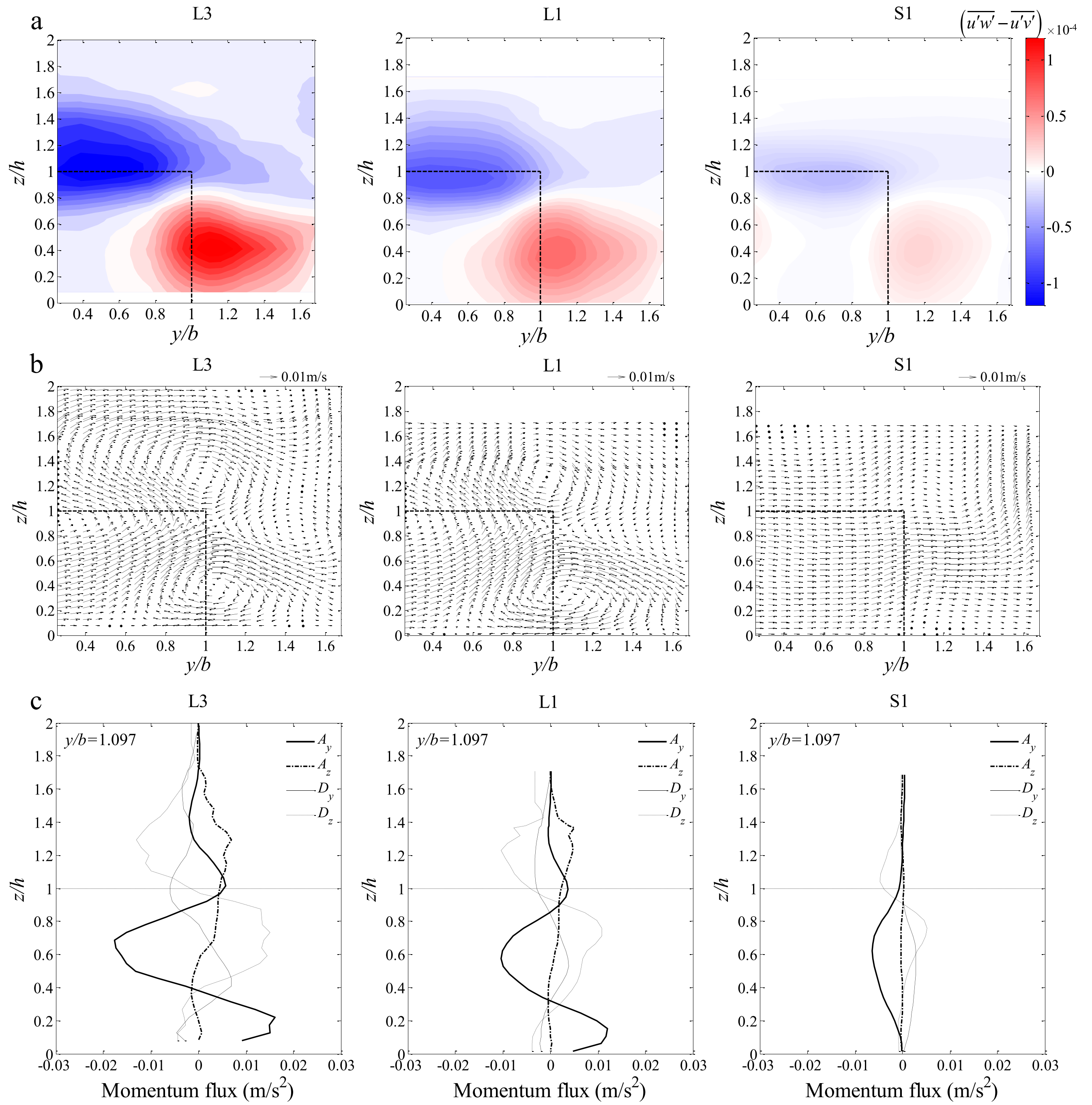

Figure 10. (a) Turbulence anisotropy characteristics, (b) Secondary flows revealed by the *V-W* vector field, and (c) vertical distributions of momentum fluxes near the junction (y/b = 1.097) under runs: L3, L1, and S1 in Supporting Information S1 (U_0 = 0.224, 0.175, and 0.177 m/s, H/h = 2.01, 1.71, and 1.67, and a = 5.56, 5.56, and 1.39 m^{-1}).

no circulation cells occur as expected due to the significant decrease in turbulence anisotropy (i.e., Figure 10a Run S1 in Supporting Information S1). Therefore, the patterns of secondary flows and turbulence anisotropy are perfectly consistent, supporting the theory of turbulence anisotropy-caused secondary flows, which are usually reported in open channel flow over roughness beds (Nezu & Nakagawa, 1993). Note that the near-bed clockwise circulation for large vegetation density enables a negative transverse velocity from the neighboring open water to the vegetation canopy above the bed. As a result, high momentum is likely to be transferred to the junction region.

However, the circulation with a positive transverse velocity also drives low momentum from the vegetation canopy to the neighboring open water. The momentum exchange processes driven by the clockwise circulation are able to account for the near-bed velocity deflection observed in this study. Also, the horizontal coherent vortices in the junction region can reduce the upper velocity above the bed. Thus, it is expected that a good argument of the significance of secondary flows and horizontal coherent vortices on the velocity deflection can be provided by an analysis of longitudinal momentum transport.

Herein, we have found that the flow structure in a partially obstructed channel with a submerged canopy is very complex due to not only the flow partitioning by vegetative drag but more importantly the mass and momentum exchange between different subregions induced by the formation of multidimensional coherent vortices and secondary flow motions. To strengthen the understanding of the momentum exchange process in the partially obstructed channel with a submerged canopy, the term-by-term momentum flux analysis is demonstrated as follows. For fully developed flows, derivatives of variables in the longitudinal direction are assumed negligible (i.e., $\partial/\partial x \approx 0$). It should be noted that this is not strictly true for flume experiments. The nonzero longitudinal gradients of variables may contribute to the momentum flux budget. For example, significant $U\partial U/\partial x$ or $-\overline{u'u'}/\partial x$ from the leading edge of the canopy mainly corresponds to the high energy slope (Moltchanov et al., 2015). However, in the sufficiently developed region, their small values do not inhibit the interpretation of how transverse or vertical motions (i.e., secondary flows and coherent vortices) contribute to the local momentum flux and thus the mean flow structure. In addition, the vegetative drag vanishes in the neighboring open water region. Therefore, the momentum equation in the longitudinal direction yields (Nezu & Onitsuka, 2001),

$$0 = \underbrace{-V\frac{\partial U}{\partial y}}_{A_y}\underbrace{-W\frac{\partial U}{\partial z}}_{A_z}\underbrace{-\frac{\partial\overline{u'v'}}{\partial y}}_{D_y}\underbrace{-\frac{\partial\overline{u'w'}}{\partial z}}_{D_z} + gS_x \tag{8}$$

In Equation 8, five terms are present to represent different physical processes of the momentum exchange. Under the effect of steady secondary flows, $A_y = -V\partial U/\partial y$ is the momentum flux due to the transverse advection and $A_z = -W\partial U/\partial z$ is the momentum flux due to the vertical advection. Under the effect of multidimensional coherent vortices, $D_y = -\partial\overline{u'v'}/\partial y$ is the momentum flux due to the transverse diffusion and $D_z = -\partial\overline{u'w'}/\partial z$ is the momentum flux due to the vertical diffusion. gS_x indicates the longitudinal component of the gravitational effect.

Figure 10c illustrates the vertical distribution of individual momentum fluxes for different canopy densities. The presented results involve a near-junction region ($y/b = 1.097$) and a far-junction region ($y/b = 1.548$). In the near-junction region, the transverse advection (A_y) and vertical diffusion (D_z) majorly contribute to the momentum budget under a large canopy density (e.g., Run L1 and Run L3 in Supporting Information S1, $a = 5.56$ m^{-1}). Near the bed ($z/h < 0.4$), positive A_y dominates the momentum exchange with $D_z \approx 0$, indicating high momentum carried by secondary flows is input in this region. For the far-bed flow layer (above $z/h = 0.4$), A_y becomes negatively pronounced, which is comparable but opposite to D_z. This indicates that vertical coherent vortices and secondary flows contribute equally to momentum exchange and compensate each other. For this layer, secondary flows transfer low momentum from the canopy region to the near-junction region and vertical coherent vortices transfer high momentum from the canopy top region to the near-junction region. Comparably, the vertical advection (A_z) and transverse diffusion (D_y) are generally much weaker but also play important roles in particular locations. For instance, positive D_y is locally peaked at $z/h = 0.4$, indicating high momentum input from the high-velocity flow. Above the canopy top ($1 < z/h < 1.4$), overall the extent of momentum exchange becomes weaker. The pronounced negative D_z and positive pronounced A_z dominate the momentum exchange. This indicates that low momentum carried by vertical coherent vortices from the lower layer is transferred to the upper layer and high momentum carried by secondary flows from the far-junction region is transferred to the junction region. For the region of $z/h > 1.4$, all terms tend to vanish. For a small canopy density (Run S1 in Supporting Information S1, $a = 1.39$ m^{-1}), all terms tend to be less significant, which are consistent with weak coherent vortices and nonformation of flow circulations. Below the canopy top ($z/h < 1$), the negative transverse advection (A_y) plays a dominant role despite the nonformation of flow circulations. Low momentum is transferred from the canopy region into the junction region by the transverse flow motion, which is compensated by positive transverse and vertical diffusions (D_y and D_z) due to weak horizontal and vertical vortices.

The vertical distribution of all terms for momentum exchange can be used for the interpretation of the performance of the near-junction velocity profiles, particularly for the velocity deflection in the near-bed region.

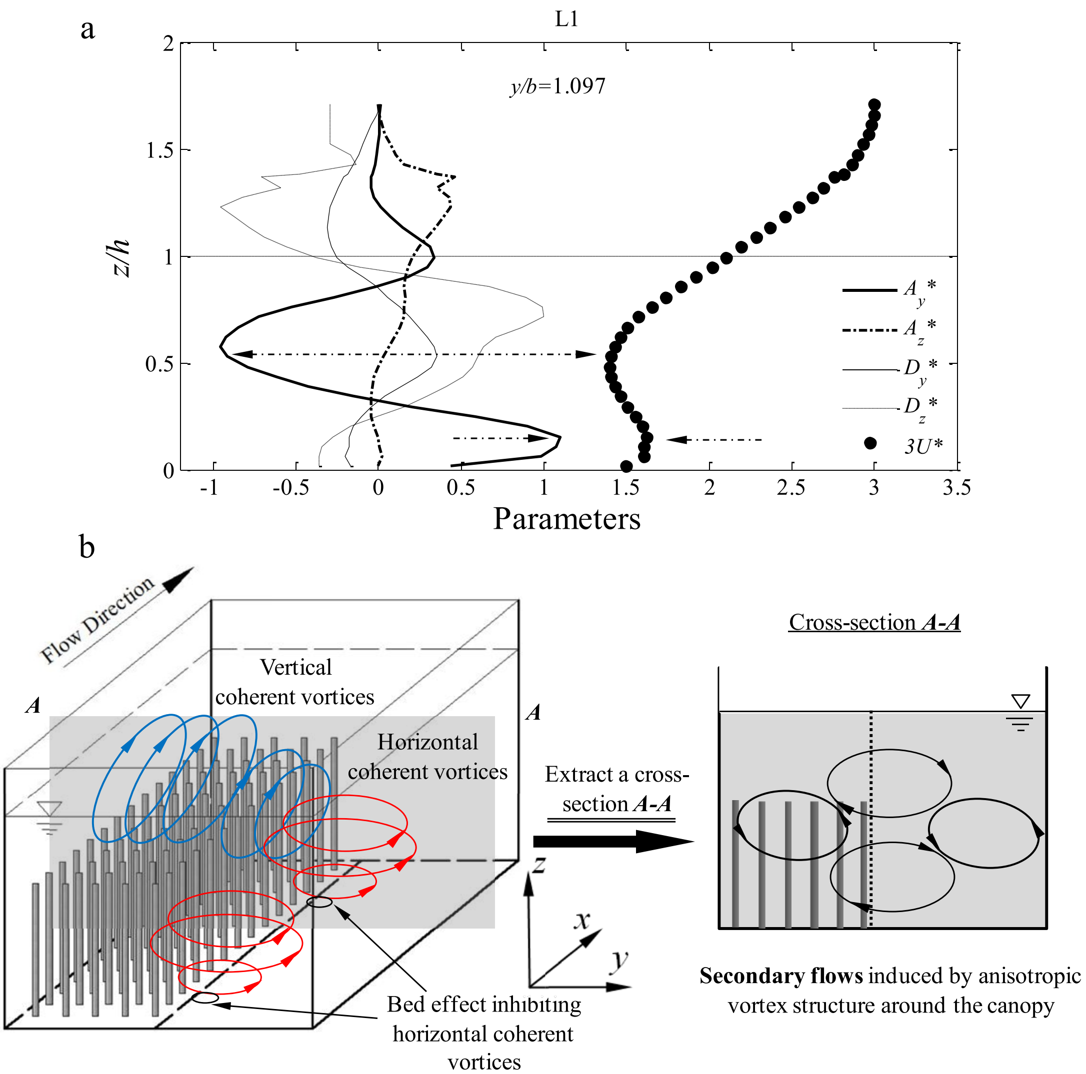

Figure 11. (a) Correspondence between vertical profiles of momentum and longitudinal velocity for L1 in Supporting Information S1 (U_0 = 0.175 m/s, H/h = 1.71, and a = 5.56 m^{-1}); different parameters with adjusted scales are plotted in one coordinate system for a better comparison. (b) Multidimensional coherent vortices and secondary flows responsible for mass and momentum exchange in a partially obstructed channel with a submerged canopy.

Figures 11a shows the correspondence between profiles of momentum fluxes and longitudinal velocity. It can be found that the near-bed velocity deflection point nicely matches the maximum of the momentum flux due to the transverse advection (A_y). This confirms that the presence of the clockwise flow circulation plays a direct role in promoting the longitudinal velocity in the near-bed region. In this region, momentum exchange due to the transverse coherent vortices is insignificant since the bed exerts an inhibitive effect on the vortex formation. Thus it can be expected that due to the presence of secondary flows the bed shear in the near junction becomes more pronounced, which tends to amplify sediment erosion in the junction region. A similar amplification of sediment erosion can be identified in flows scouring solid piles, but the amplification mechanism is attributed to the formation of dynamic large-scale vortices (e.g., horseshoe vortices; Roulund et al., 2005).

Above the deflection point (z/h = 0.2), the transverse advection starts to play a negative role for the longitudinal velocity. However, its negative impact is partially balanced by the transverse diffusion due to horizontal coherent vortices but more importantly compensated by the vertical diffusion due to vertical coherent vortices. It can be found that the local minimum velocity well corresponds to the peak magnitude of the negative transverse advection (z/h = 0.53). An interpretation can be given that secondary flows tend to decrease the longitudinal velocity but periodic vertical and transverse coherent vortices transport high momentum to the lower layer water to increase the longitudinal velocity, leading to the formation of the lower half of the hyperbolic tangent velocity

10.1029/2020WR029494

profile. The above hydrodynamic processes and performance can be well described and interpreted by the hydrodynamic model as shown in Figures 11b.

4.4. Limitation and Future Work

This study has given comprehensive quantitative descriptions of the 3D flow structure and multidimensional vortex pattern through submerged canopies. The sampling duration by the Vectrino II was comparable to previous bidimensional problems (submerged fully distributed or emergent partially distributed canopies; Caroppi et al., 2021; Zeng & Li, 2014; Zong & Nepf, 2011). It may be cautious whether the identified multidimensional (vertical and horizontal) coherent vortices can generate larger-scale coherent motions with lower frequencies or not. If so, a longer duration sampling (e.g., 10-min sampling; Ghisalberti & Nepf, 2002) of flow velocity is required to avoid the miss of larger scale vortices. The above-mentioned scenarios have been identified, for example, Wake Vortex Street of multipatch cylinder arrays (Liu et al., 2018; Yamasaki et al., 2019). In addition, the momentum exchange in the junction region has been well analyzed and discussed, which can be used to explain a particular hydrodynamic velocity behavior, namely the junction deflected velocities in the near-bed region. However, we still lack the momentum exchange performance at the scale of the entire cross section. Finally, of great interest is whether an analytical model based on the phenomenological (scaling) approach (Cheng, 2011; Ghisalberti, 2002) or momentum equation-based approach (Baptist et al., 2007; Huai et al., 2009) can simulate the vertical velocity profile in the nonvegetation side, considering that the classic tangent hyperbolic profile gradually transforms into the logarithmic profile when leaving the junction. The above-mentioned approaches will be included in our future studies.

5. Conclusions

Vegetation commonly grows partially on the channel bed and becomes submerged under high flow conditions so that three-dimensional hydrodynamic structures are generated. However, the hydrodynamics under such flow configuration were poorly understood and investigated in existing literature, leaving a knowledge gap in understanding vegetated flow behaviors and application uncertainty of existing 2D vegetated flow theory in practice. With above considerations, this study aims to explore the influence of a submerged vegetation canopy on the three-dimensional hydrodynamic structures in a partially obstructed flume. With a submerged canopy across half the bed, a number of flow and canopy configurations were designed by varying canopy density, water discharge, and water depth, which can generalize the results. Several findings are summarized as follows.

1. Dye tracer experiments were used to visualize multidimensional (vertical and horizontal) large-scale coherent vortices arising from both the top and lateral edges of the canopy, consistent with the occurrence of low-frequency peaks of PSD. Both vertical and horizontal vortices coexist near the canopy top corner, suggesting three-dimensional mass and momentum exchange
2. The three-dimensional hydrodynamics are well illustrated by the spatial patterns of longitudinal velocity, vertical and transverse Reynolds stresses, and TKE. Spatially redistributed hydrodynamics are profoundly impacted by canopy density and submergence ratio. Multidimensional flow shear layers against the top and lateral edges of the canopy form, as indicated by the distribution of longitudinal velocity and Reynolds stresses. It is shown that vertical canopy shear layer can extend outward the neighboring open water region, while the extension of transverse canopy shear layer upward the overflow layer is much weaker. Near-bed velocity deflection indicated by velocity isoline bulges is identified in the junction region, strengthened by the increase in canopy density
3. The scaling approaches for velocity and Reynolds stress regarding two-dimensional vegetated flows (either submerged flows fully covering the bed or emergent flows partially covering the bed) are examined with the three-dimensional data. It is found that the scaling approaches derived from two-dimensional flows are still applicable for highly three-dimensional flows along the canopy edges for most runs. Exceptions are found both in vertical and transverse profiles for the near-bed velocity in the junction region, where velocity deflection occurs in the vertical direction
4. Along the canopy edges, the average effect of the vertical coherent vortices overall outweighs that of the horizontal coherent vortices for dense canopies as indicated by edge-width-averaged Reynolds stresses in multidimensions. A more accurate linear relationship between the ratio of the edge-width-averaged vertical Reynolds stresses to transverse Reynolds stress and the water-related Reynolds number (Re_H) is identified with data

regression. However, the negative velocity gradient due to near-bed velocity deflection in the junction region is more closely related to the drag length-related Reynolds number (Re_{DL})

5. An in-depth analysis of secondary flows and momentum fluxes has been conducted to show the mass and momentum exchange processes in the junction region. The results show that secondary flow circulations are generated due to the anisotropy in turbulence (multidimensional coherent vortices), governing the momentum advection including the domination in near-bed momentum input and the compensation to the far-bed momentum input provided by vertical coherent vortices in the junction region. These momentum exchange processes can be used to understand the three-dimensional hydrodynamics such as velocity deflections and deviations of scaled longitudinal velocities from the flow shear layer in the near-bed region

Conflict of Interest

The authors declare no conflicts of interest relevant to this study.

Data Availability Statement

Relevant video and data results of this article are available at https://doi.org/10.5281/zenodo.4362495.

Acknowledgments
This research was supported by the National Natural Science Foundation of China (51,639,007, 51,909,178 and 41,771,543) and the Open Foundation project (SKHL1913, SKHL1804), State Key Laboratory of Hydraulics and Mountain River Engineering, Sichuan University. Relevant video and data results of this article are available at https://doi.org/10.5281/zenodo.4362495.

References

Bao, M., & Li, C. (2017). Hydrodynamics and bed stability of open channel flows with submerged foliaged plants. *Environmental Fluid Mechanics*, *17*(4), 815–831. https://doi.org/10.1007/s10652-017-9524-1

Baptist, M., Babovic, V., Rodríguez Uthurburu, J., Keijzer, M., Uittenbogaard, R., Mynett, A., & Verwey, A. (2007). On inducing equations for vegetation resistance. *Journal of Hydraulic Research*, *45*(4), 435–450. https://doi.org/10.1080/00221686.2007.9521778

Bennett, S. J., Pirim, T., & Barkdoll, B. D. (2002). Using simulated emergent vegetation to alter stream flow direction within a straight experimental channel. *Geomorphology*, *44*(1–2), 115–126. https://doi.org/10.1016/s0169-555x(01)00148-9

Blanckaert, K., & Graf, W. H. (2001). Mean flow and turbulence in open-channel bend. *Journal of Hydraulic Engineering*, *127*(10), 835–847. https://doi.org/10.1061/(asce)0733-9429(2001)127:10(835)

Caroppi, G., Västilä, K., Gualtieri, P., Järvelä, J., Giugni, M., & Rowiński, P. M. (2021). Comparison of flexible and rigid vegetation induced shear layers in partly vegetated channels. *Water Resources Research*, *57*(3), e2020WR028243. https://doi.org/10.1029/2020wr028243

Caroppi, G., Västilä, K., Järvelä, J., Rowiński, P. M., & Giugni, M. (2019). Turbulence at water-vegetation interface in open channel flow: Experiments with natural-like plants. *Advances in Water Resources*, *127*, 180–191. https://doi.org/10.1016/j.advwatres.2019.03.013

Chanson, H., Trevethan, M., & Koch, C. (2007). Discussion of "turbulence measurements with acoustic Doppler velocimeters" by Carlos M. García, Mariano I. Cantero, Yarko Niño, and Marcelo H. García. *Journal of Hydraulic Engineering*, *133*(11), 1286–1289. https://doi.org/10.1061/(asce)0733-9429(2007)133:11(1283)

Chen, Z., Ortiz, A., Zong, L., & Nepf, H. (2012). The wake structure behind a porous obstruction and its implications for deposition near a finite patch of emergent vegetation. *Water Resources Research*, *48*(9), W09517. https://doi.org/10.1029/2012wr012224

Cheng, N.-S. (1997). Simplified settling velocity formula for sediment particle. *Journal of Hydraulic Engineering*, *123*(2), 149–152. https://doi.org/10.1061/(asce)0733-9429(1997)123:2(149)

Cheng, N. S. (2011). 2011 Representative roughness height of submerged vegetation. *Water Resources Research*, *47*, 1–18.

Cheng, N.-S., & Nguyen, H. T. (2011). Hydraulic radius for evaluating resistance induced by simulated emergent vegetation in open-channel flows. *Journal of Hydraulic Engineering*, *137*(9), 995–1004. https://doi.org/10.1061/(asce)hy.1943-7900.0000377

Choi, S.-U., & Kang, H. (2006). Numerical investigations of mean flow and turbulence structures of partly-vegetated open-channel flows using the Reynolds stress model. *Journal of Hydraulic Research*, *44*(2), 203–217. https://doi.org/10.1080/00221686.2006.9521676

Choi, S.-U., & Kang, H. (2016). Characteristics of mean flow and turbulence statistics of depth-limited flows with submerged vegetation in a rectangular open-channel. *Journal of Hydraulic Research*, *54*(5), 527–540. https://doi.org/10.1080/00221686.2016.1168882

Devi, T. B., & Kumar, B. (2016). Flow characteristics in an alluvial channel covered partially with submerged vegetation. *Ecological Engineering*, *94*, 478–492. https://doi.org/10.1016/j.ecoleng.2016.06.018

Dunn, C. (1996). *Experimental determination of drag coefficients in open channel with simulated vegetation*. MS Thesis, University of Illinois at Urbana-Champaign.

Etminan, V., Lowe, R. J., & Ghisalberti, M. (2017). A new model for predicting the drag exerted by vegetation canopies. *Water Resources Research*, *53*(4), 3179–3196. https://doi.org/10.1002/2016wr020090

Ghisalberti, M. (2002). Mixing layers and coherent structures in vegetated aquatic flows. *Journal of Geophysical Research*, *107*, 3011. https://doi.org/10.1029/2001jc000871

Ghisalberti, M., & Nepf, H. M. (2002). Mixing layers and coherent structures in vegetated aquatic flows. *Journal of Geophysical Research: Oceans*, *107*, 3011. https://doi.org/10.1029/2001jc000871

Ghisalberti, M., & Nepf, H. M. (2004). The limited growth of vegetated shear layers. *Water Resources Research*, *40*(7), W07502. https://doi.org/10.1029/2003wr002776

Goring, D. G., & Nikora, V. I. (2002). Despiking acoustic Doppler velocimeter data. *Journal of Hydraulic Engineering*, *128*(1), 117–126. https://doi.org/10.1061/(asce)0733-9429(2002)128:1(117)

Guo, J., Jiang, W., & Chen, G. (2020). Transient solute dispersion in wetland flows with submerged vegetation: An analytical study in terms of time-dependent properties. *Water Resources Research*, *56*(2), e2019WR025586. https://doi.org/10.1029/2019wr025586

He, G., Han, X., Fang, H., Reible, D., & Huang, L. (2019). Effects of roughness Reynolds number on scalar transfer mechanisms at the sediment-water interface. *Water Resources Research*, *55*(8), 6811–6824. https://doi.org/10.1029/2018wr024493

Horstman, E., Bryan, K., Mullarney, J., Pilditch, C., & Eager, C. (2018). Are flow-vegetation interactions well represented by mimics? A case study of mangrove pneumatophores. *Advances in Water Resources*, *111*, 360–371. https://doi.org/10.1016/j.advwatres.2017.11.018

Huai, W., Xue, W., & Qian, Z. (2015). Large-eddy simulation of turbulent rectangular open-channel flow with an emergent rigid vegetation patch. *Advances in Water Resources*, *80*, 30–42. https://doi.org/10.1016/j.advwatres.2015.03.006

Huai, W., Yang, L., & Guo, Y. (2020). Analytical solution of suspended sediment concentration profile: Relevance of dispersive flow term in vegetated channels. *Water Resources Research*, *56*(7), e2019WR027012. https://doi.org/10.1029/2019wr027012

Huai, W., Zeng, Y., Xu, Z., & Yang, Z. (2009). Three-layer model for vertical velocity distribution in open channel flow with submerged rigid vegetation. *Advances in Water Resources*, *32*(4), 487–492. https://doi.org/10.1016/j.advwatres.2008.11.014

Huai, W.-X., Zhang, J., Wang, W.-J., & Katul, G. G. (2019). Turbulence structure in open channel flow with partially covered artificial emergent vegetation. *Journal of Hydrology*, *573*, 180–193. https://doi.org/10.1016/j.jhydrol.2019.03.071

Jordanova, A. A., & James, C. (2003). Experimental study of bed load transport through emergent vegetation. *Journal of Hydraulic Engineering*, *129*(6), 474–478. https://doi.org/10.1061/(asce)0733-9429(2003)129:6(474)

Kim, H. S., Kimura, I., & Shimizu, Y. (2015). Bed morphological changes around a finite patch of vegetation. *Earth Surface Processes and Landforms*, *40*(3), 375–388. https://doi.org/10.1002/esp.3639

Kothyari, U. C., Hayashi, K., & Hashimoto, H. (2009). Drag coefficient of unsubmerged rigid vegetation stems in open channel flows. *Journal of Hydraulic Research*, *47*(6), 691–699. https://doi.org/10.3826/jhr.2009.3283

Le Bouteiller, C., & Venditti, J. (2015). Sediment transport and shear stress partitioning in a vegetated flow. *Water Resources Research*, *51*(4), 2901–2922. https://doi.org/10.1002/2014wr015825

Li, C., & Wang, J. (2002). Large eddy simulation of dispersion in free surface shear flow. *Journal of Hydraulic Research*, *40*(3), 351–358. https://doi.org/10.1080/00221680209499949

Li, C.-w., & Busari, A. O. (2019). Hybrid modeling of flows over submerged prismatic vegetation with different areal densities. *Engineering Applications of Computational Fluid Mechanics*, *13*(1), 493–505. https://doi.org/10.1080/19942060.2019.1610501

Li, C. W., & Zeng, C. (2009). 3D Numerical modelling of flow divisions at open channel junctions with or without vegetation. *Advances in Water Resources*, *32*(1), 49–60. https://doi.org/10.1016/j.advwatres.2008.09.005

Liu, C., Hu, Z., Lei, J., & Nepf, H. (2017). Vortex structure and sediment deposition in the wake behind a finite patch of model submerged vegetation. *Journal of Hydraulic Engineering*, *144*(2), 04017065. https://doi.org/10.1061/(asce)hy.1943-7900.0001408

Liu, C., Hu, Z., Lei, J., & Nepf, H. (2018). Vortex structure and sediment deposition in the wake behind a finite patch of model submerged vegetation. *Journal of Hydraulic Engineering*, *144*(2), 04017065. https://doi.org/10.1061/(asce)hy.1943-7900.0001408

Liu, C., & Nepf, H. (2016). Sediment deposition within and around a finite patch of model vegetation over a range of channel velocity. *Water Resources Research*, *52*(1), 600–612. https://doi.org/10.1002/2015wr018249

Liu, D., Diplas, P., Fairbanks, J. D., & Hodges, C. C. (2008). An experimental study of flow through rigid vegetation. *Journal of Geophysical Research*, *113*, F04015. https://doi.org/10.1029/2008jf001042

Liu, D., Valyrakis, M., & Williams, R. (2017). Flow hydrodynamics across open channel flows with riparian zones: Implications for riverbank stability. *Water*, *9*, 720. https://doi.org/10.3390/w9090720

Meftah, M. B., De Serio, F., & Mossa, M. (2014). Hydrodynamic behavior in the outer shear layer of partly obstructed open channels. *Physics of Fluids*, *26*(6), 065102. https://doi.org/10.1063/1.4881425

Meftah, M. B., & Mossa, M. (2016). Partially obstructed channel: Contraction ratio effect on the flow hydrodynamic structure and prediction of the transversal mean velocity profile. *Journal of Hydrology*, *542*, 87–100. https://doi.org/10.1016/j.jhydrol.2016.08.057

Moltchanov, S., Bohbot-Raviv, Y., Duman, T., & Shavit, U. (2015). Canopy edge flow: A momentum balance analysis. *Water Resources Research*, *51*(4), 2081–2095. https://doi.org/10.1002/2014wr015397

Murphy, E., Ghisalberti, M., & Nepf, H. (2007). *Model and Laboratory Study of Dispersion in Flows with Submerged Vegetation* (Vol. 43). Water Resources Research.

Neary, V. S., Constantinescu, S. G., Bennett, S. J., & Diplas, P. (2012). Effects of vegetation on turbulence, sediment transport, and stream Morphology. *Journal of Hydraulic Engineering*, *138*(9), 765–776. https://doi.org/10.1061/(asce)hy.1943-7900.0000168

Nepf, H., & Vivoni, E. (2000). Flow structure in depth-limited, vegetated flow. *Journal of Geophysical Research: Oceans*, *105*, 28547–28557. https://doi.org/10.1029/2000jc900145

Nepf, H. M. (2012). Hydrodynamics of vegetated channels. *Journal of Hydraulic Research*, *50*(3), 262–279. https://doi.org/10.1080/00221686.2012.696559

Nezu, I., & Nakagawa, H. (1993). *Turbulence in open channel flows*. IAHR. Balkema.

Nezu, I., & Onitsuka, K. (2001). Turbulent structures in partly vegetated open-channel flows with LDA and PI V measurements. *Journal of Hydraulic Research*, *39*(6), 629–642. https://doi.org/10.1080/00221686.2001.9628292

Poggi, D., Porporato, A., Ridolfi, L., Albertson, J., & Katul, G. (2004). The effect of vegetation density on canopy sub-layer turbulence. *Bound-Lay Meteorol*, *111*(3), 565–587. https://doi.org/10.1023/b:boun.0000016576.05621.73

Risse-Buhl, U., Anlanger, C., Kalla, K., Neu, T. R., Noss, C., Lorke, A., & Weitere, M. (2017). The role of hydrodynamics in shaping the composition and architecture of epilithic biofilms in fluvial ecosystems. *Water Research*, *127*, 211–222. https://doi.org/10.1016/j.watres.2017.09.054

Rominger, J. T., & Nepf, H. M. (2011). Flow adjustment and interior flow associated with a rectangular porous obstruction. *Journal of Fluid Mechanics*, *680*, 636–659. https://doi.org/10.1017/jfm.2011.199

Roulund, A., Sumer, B. M., Fredsøe, J., & Michelsen, J. (2005). Numerical and experimental investigation of flow and scour around a circular pile. *Journal of Fluid Mechanics*, *534*, 351–401. https://doi.org/10.1017/s0022112005004507

Rubol, S., Battiato, I., & de Barros, F. P. (2016). Vertical dispersion in vegetated shear flows. *Water Resources Research*, *52*(10), 8066–8080. https://doi.org/10.1002/2016wr018907

Shucksmith, J., Boxall, J., & Guymer, I. (2011). Determining longitudinal dispersion coefficients for submerged vegetated flow. *Water Resources Research*, *47*(10). https://doi.org/10.1029/2011wr010547

Su, X., & Li, C. W. (2002). Large eddy simulation of free surface turbulent flow in partly vegetated open channels. *International Journal for Numerical Methods in Fluids*, *39*(10), 919–937. https://doi.org/10.1002/fld.352

Truong, S., Uijttewaal, W., & Stive, M. (2019). Exchange processes induced by large horizontal coherent structures in floodplain vegetated channels. *Water Resources Research*, *55*(3), 2014–2032. https://doi.org/10.1029/2018wr022954

Wang, H.-z., Xu, Z.-x., Yu, H.-t., & Wang, X.-k. (2018). Flow variability along a vegetated natural stream under various sediment transport rates. *Journal of Mountain Science*, *15*(11), 2347–2364. https://doi.org/10.1007/s11629-018-4835-3

White, B. L., & Nepf, H. M. (2007). Shear instability and coherent structures in shallow flow adjacent to a porous layer. *Journal of Fluid Mechanics*, *593*, 1–32. https://doi.org/10.1017/s0022112007008415

Xu, Z.-X., Ye, C., Zhang, Y.-Y., Wang, X.-K., & Yan, X.-F. (2019). *2D numerical analysis of the influence of near-bank vegetation patches on the bed morphological adjustment* (pp. 1–32). Environmental Fluid Mechanics.

Yamasaki, T. N., de Lima, P. H., Silva, D. F., Cristiane, G. A., Janzen, J. G., & Nepf, H. M. (2019). From patch to channel scale: The evolution of emergent vegetation in a channel. *Advances in Water Resources*, *129*, 131–145. https://doi.org/10.1016/j.advwatres.2019.05.009

Yan, X. F., Wai, W. H. O., & Li, C. W. (2016). Characteristics of flow structure of free-surface flow in a partly obstructed open channel with vegetation patch. *Environmental Fluid Mechanics*, *16*(4), 807–832. https://doi.org/10.1007/s10652-016-9453-4

Yang, J. Q., Kerger, F., & Nepf, H. M. (2015). Estimation of the bed shear stress in vegetated and bare channels with smooth beds. *Water Resources Research*, *51*(5), 3647–3663. https://doi.org/10.1002/2014wr016042

Yang, K., Cao, S., & Knight, D. W. (2007). Flow patterns in compound channels with vegetated floodplains. *Journal of Hydraulic Engineering*, *133*(2), 148–159. https://doi.org/10.1061/(asce)0733-9429(2007)133:2(148)

Yang, S.-Q., Tan, S.-K., & Lim, S.-Y. (2004). Velocity distribution and dip-phenomenon in smooth uniform open channel flows. *Journal of Hydraulic Engineering*, *130*(12), 1179–1186. https://doi.org/10.1061/(asce)0733-9429(2004)130:12(1179)

Yang, Z., Li, D., Huai, W., & Liu, J. (2019). A new method to estimate flow conveyance in a compound channel with vegetated floodplains based on energy balance. *Journal of Hydrology*, *575*, 921–929. https://doi.org/10.1016/j.jhydrol.2019.05.078

Zeng, C., & Li, C. (2012). Modeling flows over gravel beds by a drag force method and a modified S–A turbulence closure. *Advances in Water Resources*, *46*, 84–95. https://doi.org/10.1016/j.advwatres.2012.02.001

Zeng, C., & Li, C. W. (2014). Measurements and modeling of open-channel flows with finite semi-rigid vegetation patches. *Environmental Fluid Mechanics*, *14*(1), 113–134. https://doi.org/10.1007/s10652-013-9298-z

Zong, L., & Nepf, H. (2011). *Vortex development behind a finite porous obstruction in a channel*.